Remote Sensing of Environment 277 (2022) 113075

Contents lists available at ScienceDirect

Remote Sensing of Environment

journal homepage: www.elsevier.com/locate/rse

Simulation of solar-induced chlorophyll fluorescence by modeling radiative coupling between vegetation and atmosphere with WPS

Feng Zhao [a,*], Zhenjiang Li [a], Wout Verhoef [b], Chongrui Fan [a,c], Hexuan Luan [a], Tiangang Yin [d], Jian Zhang [e], Zhunqiao Liu [f], Chiming Tong [g], Yunfei Bao [g]

[a] School of Instrumentation Science and Opto-Electronics Engineering, Beihang University, Beijing 100191, PR China
[b] Faculty of Geo-information Science and Earth Observation (ITC), University of Twente, P.O. Box 217, Enschede 7500 AE, the Netherlands
[c] Department of Computing, Imperial College London, South Kensington Campus London, SW7 2AZ, UK
[d] Earth System Science Interdisciplinary Center, University of Maryland, College Park, MD 20740-3823, USA
[e] Macro Agriculture Research Institute, College of Resources and Environment, Huazhong Agricultural University, Wuhan 430070, PR China
[f] State Key Laboratory of Soil Erosion and Dryland Farming on the Loess Plateau, Northwest A&F University, Yangling, Shaanxi 712100, PR China
[g] Beijing Institute of Space Mechanics and Electricity, China Academy of Space Technology, Beijing 100094, PR China

ARTICLE INFO

Edited by Jing M. Chen

Keywords:
Solar-induced chlorophyll fluorescence (SIF)
Radiative transfer modeling
Monte Carlo ray-tracing (MCRT)
WPS (weighted photon spread)
Radiative coupling between atmosphere and land surface
Three-dimensional (3-D) canopies
Model intercomparison

ABSTRACT

Recent advances in instruments and retrieval methods enable measurements of solar-induced chlorophyll fluorescence (SIF) across a wide range of scales. Radiative transfer (RT) models for simulating scattering and (re-) absorption of SIF provide a powerful tool to study the upscaling of SIF signal from leaf level to terrestrial ecosystems. Based on the Monte Carlo ray-tracing (MCRT) model, WPS (Weighted Photon Spread), we made major extensions with new functionalities and systematic evaluation of the new modules. By modeling the radiative coupling between atmosphere and land surface with the same MCRT method, the non-fluorescent and SIF radiance received by sensors can be simulated at levels from top-of canopy to top-of-atmosphere (TOA) in a coherent manner. New extension to represent the three-dimensional (3-D) canopies with geometrical primitives composed of turbid medium makes the hyperspectral simulation (especially SIF) for a sensor with medium spatial resolution at kilometer-scale feasible and practical. Evaluations through ROMC (Radiation transfer model intercomparison Online Model Checker) show that the accuracy of the new module of 3-D structure representation in WPS is within 1% of the reference solution. The spectra of TOA radiance and SIF and their components simulated at nadir by WPS agree closely with those simulated by the coupled SCOPE and MODTRAN models with the coefficient of determination (R^2) higher than 0.99 and the average absolute relative error (AARE) lower than 6.39%; for angular distributions of TOA radiance and SIF at 685 nm and 740 nm, R^2 is higher than 0.81 and AARE is lower than 6.94%. Comparisons of the spectra of TOA radiance and SIF and their components simulated at nadir by WPS and the DART model give R^2 higher than 0.99 and AARE lower than 3.5%; R^2 is higher than 0.92 and AARE is lower than 5.92% for the TOA angular simulations. The WPS model was also evaluated by hyperspectral measurements through unmanned aerial vehicle at different altitudes, which shows that WPS can reproduce the spectral features of a rapeseed crop. WPS can be used as a versatile tool to assess the impacts of various factors on the SIF signal and to evaluate the SIF retrieval methods under different conditions.

1. Introduction

Some of the solar photons absorbed by the pigments (mainly chlorophyll) in plant leaves are emitted at longer wavelengths as fluorescence, known as solar-induced chlorophyll fluorescence (SIF). Because of its close link to photosynthetic activity, SIF can serve as a direct and non-invasive indicator of the functioning and status of vegetation (Frankenberg and Berry, 2018). Remote sensing of SIF is a rapidly advancing front with diverse applications in terrestrial vegetation (Mohammed et al., 2019) and marine systems with algal species (Gupana et al., 2021).

Recent advances in instruments and retrieval methods enable fluorescence measurements across a wide range of scales from leaf level to terrestrial ecosystems (Zhao et al., 2018b; Mohammed et al., 2019;

* Corresponding author.
E-mail address: zhaofeng@buaa.edu.cn (F. Zhao).

https://doi.org/10.1016/j.rse.2022.113075
Received 14 July 2021; Received in revised form 15 April 2022; Accepted 2 May 2022
Available online 12 May 2022

Porcar-Castell et al., 2021). Emission of chlorophyll fluorescence inside the photosynthetic apparatus is influenced directly or indirectly by biological and environmental factors (Porcar-Castell et al., 2014). However, when scaling the SIF signal upwards from leaf scale, these factors tend to be averaged out in large footprints (Mohammed et al., 2019), exemplified as a nonlinear relationship between SIF and gross primary production at leaf level, in contrast with the linear correlation found at global scale (Frankenberg and Berry, 2018). To circumvent limitations in our ability to study plant systems across different scales, it is common to use mathematical models to translate information obtained at one scale to another scale of interest where data are lacking (Bailey, 2019). Mathematical models have been developed for the quantitative description of various drivers and fluorescence, including leaf physiological models of fluorescence excitation, radiative transfer (RT) models for simulating scattering and (re-)absorption of SIF inside the leaf and canopy, and integrated modeling of canopy SIF and photosynthesis with both the radiative fluxes and non-radiative energy fluxes. For a review of these models, refer to Mohammed et al. (2019). However, before enabling the full potential of upscaling of SIF from the leaf to the ecosystem, a number of challenges must be overcome. Among the challenging issues, the impact of the canopy structural heterogeneity on the RT of SIF and the influence of atmospheric gases and aerosols on large-scale remote sensing SIF observations are still poorly considered in existing SIF models (Porcar-Castell et al., 2021).

In the framework of the FluorMOD project, the FluorSAIL model was developed to simulate the RT of SIF inside a one-dimensional (1-D) canopy (Miller et al., 2005), based on one of the most widely used analytic RT models, SAIL (Scattering by Arbitrarily Inclined Leaves) (Verhoef, 1984). FluorSAIL was extended to integrate RT of leaf and canopy, photosynthesis and energy balance calculations, resulting in the model called SCOPE (Soil Canopy Observation, Photochemistry and Energy fluxes) (van der Tol et al., 2009). By allowing vertical variations of leaf optical properties and canopy structural parameters, Yang et al. (2017) further extended the SCOPE model into the mSCOPE model that can represent the canopy as vertically heterogeneous layers. These models are all based on the classic four-stream RT theory (Verhoef, 1985), which is a reasonable approximation of the flux field for horizontally homogeneous 1-D canopies.

Since the RT of excited fluorescence is essentially the same as that for non-fluorescent radiation within the canopy, some numerical methods of the RT problem to model canopy reflectance were also applied for canopy SIF modeling. The Monte Carlo ray-tracing (MCRT) method offers a flexible yet physically rigorous approach to photon transport in a plant canopy of arbitrarily structural complexity. According to the method to represent the plant canopy, two sub-categories can be further divided for forward MCRT. If the elements of the plant canopy, e.g., leaves, stems, stalks, branches, and background, are all explicitly represented by a number of facets ("explicit canopy"' for short), tracing of the photon is solely determined by ray and objects (facets) intersection testing. Another method abstracts the plants as volumetric primitives composed of turbid medium ("turbid canopy"), in which the traveling distance and scattering direction of the photon are randomly sampled according to various probability density functions. The FluorWPS model (Zhao et al., 2016) belongs to the first kind of forward MCRT models above mentioned to simulate top-of-canopy (TOC) SIF, which is an extension of the Weighted Photon Spread (WPS) model (Zhao et al., 2015) by combining the photon spread method and the weight reduction concept to simulate TOC bidirectional reflectance of explicit canopy. Since the turbid canopy abstraction can greatly simplify the scene representation for highly heterogeneous vegetation canopies and hence significantly reduce the computer memory and time, models like FLIGHT (North, 1996) and FLiES (Kobayashi and Iwabuchi, 2008) adopt the second kind of MCRT approach to simulate bidirectional reflectance of 3-D canopies, with the advantage of a high efficiency for large-scale forest canopies. Inclusion of simulating the RT of SIF into these two models resulted in the FluorFLIGHT (Hernández-Clemente et al., 2017) and FLiES-SIF (Sakai et al., 2020) models, respectively. Besides the MCRT method, another widely used computer rendering technique, the radiosity method, was introduced for the canopy reflectance modeling (Borel et al., 1991; Goel et al., 1991) and also extended for canopy SIF modeling for explicit canopy (Zhao et al., 2018a).

The Discrete Anisotropic Radiative Transfer (DART) model (Gastellu-Etchegorry et al., 1996) simulates canopy reflectance of 3-D scenes with the discrete ordinate method, wherein tracking of the flux propagation is restricted to a finite number of directions. Recently, the similar flux tracking method was used to trace fluorescent fluxes that originate from the leaves and finally to simulate the SIF signal observed by a sensor at TOC or top-of-atmosphere (TOA) level (Gastellu-Etchegorry et al., 2017; Malenovský et al., 2021).

By adapting the theory of canopy spectral invariants (so called '*p*-theory'), Zeng et al. (2020) developed a semi-analytical SIF model based on canopy escape and recollision probabilities, with the capability of TOC SIF simulations for both homogeneous and heterogeneous canopies. It is worth noting that the *p*-theory can be applied to infer the total emitted SIF of the canopy from TOC observed SIF in the far-red band (Liu et al., 2018; Yang and van der Tol, 2018), with the former showing stronger correlation with gross primary production (Lu et al., 2020).

It can be seen that the simulation of canopy SIF within the canopy has been successfully implemented for several major solutions of the canopy RT problem. With the coupling of a leaf-level fluorescence emission and optical property model, which is mostly the Fluspect model (Vilfan et al., 2016) or its updates (van der Tol et al., 2019), the canopy RT formulations can upscale the emitted fluorescence to the SIF signal observed at TOC. SIF at TOA can be further simulated if radiative coupling of the "surface - atmosphere" system is properly modeled. The capability of modeling the atmospheric absorption and scattering of SIF between the canopy and sensor is especially important since SIF traveling towards the sensor experiences the same atmospheric attenuation upon which some of the SIF retrieval methods are based. SIF retrievals from hyperspectral observations based on platforms of tower (Daumard et al., 2010; Sabater et al., 2018), UAV (Garzonio et al., 2017), aircraft (e.g., Damm et al., 2014; Daumard et al., 2015; Rascher et al., 2015), and satellite (Frankenberg and Berry, 2018) highlight the complexity of atmospheric interferences. There are additional complications, namely, the complex interplay between changing surface properties (i.e., structure and anisotropy) and atmospheric effects. Physically based models that are capable of simulating radiative coupling between vegetation and atmosphere can help to elucidate the SIF signal retrieved from remote observations.

Among the RT models mentioned above, the SCOPE (by coupling with the MODTRAN model) and DART models can further simulate the transfer of TOC SIF up towards a sensor at TOA. Based on the four-stream RT theory, the SCOPE (or its precursor SAIL) and MODTRAN models were coupled to simulate upward non-fluorescent radiance and SIF at TOA (Cogliati et al., 2015; Verhoef and Bach, 2007, 2012; Verhoef et al., 2018). The modeling of the canopy-atmosphere directional effects within the four-stream framework was realized by considering the four reflectance terms of the canopy and their coupling with the atmospheric functions. The coupled SCOPE and MODTRAN models represent the state-of-art scheme to depict the RT interactions of the Earth's surface-atmosphere system for horizontally continuous medium. The atmosphere in DART is simulated as the vertical and horizontal juxtaposition of air cells, by taking into account the vertical distribution of gasses and aerosols. The atmosphere RT module works on the same basis as DART, i.e. the discrete ordinate method with the flux tracking approach (Grau and Gastellu-Etchegorry, 2013). With the atmosphere characteristics inputted manually or built-in atmosphere databases generated by the MODTRAN model, non-fluorescent radiance and SIF spectra at TOA can be simulated by the DART model. Although the coupled SCOPE and MODTRAN models have been extensively applied to generate datasets including TOA radiance and SIF for testing the SIF retrieval approaches (e.g., Cogliati et al., 2015; Verhoef et al., 2018; Zhao et al., 2022), the

vegetation is represented as 1-D layer(s) in which fluxes only in the vertical direction are considered. The atmosphere module in DART is originally developed for the simulation of TOA non-fluorescent radiance. It is not known about the performance of applying DART for simulating TOA SIF. To the best of our knowledge, no attempts have been reported in scientific literature for comparing and evaluating the accuracy and reliability of the RT solutions to the coupled surface-atmosphere system to model TOA radiance with SIF. Meanwhile, there is increasing demand of studying the RT of SIF for complex 3-D canopies with horizontal and vertical heterogeneity (e.g., Liu et al., 2019; Hornero et al., 2021; Tong et al., 2021). Accordingly, the requirement on computer resources will also increase, because 3-D SIF RT models that resolve plant level heterogeneity often incur a significant computational cost. Therefore, the improvement of computational efficiency in terms of simulation time and computer memory for the 3-D SIF RT models is also an important issue by considering that high-performance computer resources are not commonly available.

Recently we extended the WPS model by considering the radiative coupling between the atmosphere and the land surface to simulate the SIF signal received by sensors from TOC up until TOA. Besides, to avoid extensive computer memory and computational time required to simulate RT in architecturally realistic 3-D canopies explicitly represented by large numbers of facets, we adopted geometrical primitives composed of turbid medium to describe complex 3-D plant structures, i.e. the turbid canopy abstraction. Accordingly, approaches were implemented to simulate ray propagation and interaction for the turbid canopy representation of a 3-D vegetative scene. In this study, on the basis of improvement and extension of the WPS model, we performed an initial intercomparison between it and other two SIF RT models, i.e. SCOPE and DART, at both TOC and TOA levels. The rest of the paper is organized as follows: in Section 2, the extended WPS model and the datasets used for the evaluation of the model in this study are described; the intercomparison and evaluation of the WPS model are performed in Section 3; comparison results and discussions are presented in Section 4; Section 5 gives the concluding remarks.

2. Description of the WPS model

2.1. The radiative transfer equation

The RT theory of light propagation in a medium has been successfully applied for solving problems in various fields, e.g., astrophysics, atmospheric physics, and vegetation radiation regime (Chandrasekhar, 1950; Ishimaru, 1978; Ross, 1981).The heart of this theory is the radiative transfer equation (RTE) (in monochromatic form):

$$sin\theta cos\varphi \frac{\partial L(r,\Omega)}{\partial x} + sin\theta sin\varphi \frac{\partial L(r,\Omega)}{\partial y} + cos\theta \frac{\partial L(r,\Omega)}{\partial z} + \sigma(r,\Omega)L(r,\Omega) = \int_{4\pi} L(r,\Omega')\sigma_s(r,\Omega'\rightarrow\Omega)d\Omega' + Q_s(r,\Omega) \quad (1)$$

where L is the radiance at position r in the direction Ω in a three-dimensional space. The RTE represents a balance equation for radiative energy in an infinitesimal volume element in which the effects of absorption ($\sigma_a = \sigma - \sigma_s$) and scattering ($\sigma_s$) need to be considered, with σ the extinction or total interaction coefficient. Q_s represents the external or internal radiation source, which is fluorescence emission by vegetative elements in this study.

Approaches that solve the RTE in atmosphere or canopies have been developed with varying degrees of complexity and accuracy (Liou, 2002; Kuusk, 2018). Before applying them for the coupled system of 1-D atmosphere and 3-D vegetation canopy considered here, some key differences for the two subsystems should be noted. (1) In contrast with the isotropic scattering coefficient σ_s for atmospheric media that is only dependent on the scattering angle between the incoming and outgoing directions of photon travel, σ_s for vegetative elements generally depends upon the absolute directions of photon travel (Shultis and Myneni, 1988), because of the orientation of the vegetative elements imposed by the force of gravity. As a result, discrete ordinates method widely used in atmospheric RT models cannot be easily combined with a canopy reflectance model. (2) The size of vegetative scatterers is much larger than the molecules and aerosol particles of air, and also to the wavelength of the incident solar radiation, which results in the hotspot effect in the bidirectional reflectance of vegetation (Kuusk, 1991). Nevertheless, this effect does not need to be considered in atmospheric RT modeling. (3) Unlike the top of the atmosphere, the canopy is exposed both to the direct sunlight and the diffused radiation from the sky, leading to a more complex upper boundary condition for the canopy RT model. This problem of specifying the correct boundary condition at the atmosphere-canopy interface can be eliminated with a coupled RT modeling of atmosphere and canopy as adopted in this study. (4) The typical spatial scale is quite different between atmosphere (10–1000 km^2) and canopy (0.01–1 km^2) models (Kobayashi and Iwabuchi, 2008). Therefore, the atmosphere can be usually treated as a continuous turbid medium under clear weather conditions, whereas vegetative canopies are generally represented as heterogeneous and complex 3-D scene at the kilometer scale and beyond. Therefore a scenario of coupled 1-D atmospheric layers with 3-D canopies is assumed here for the RT simulations as a first step.

The RTE gives a quantitative description of the RT in a scattering medium composed of discrete scatterers which determine the scattering and absorption properties of the medium, without explicitly considering the discreteness of the scatterers. On the other hand, the RT problem can also be solved by directly simulating the chain of photon collisions with the discrete scatterers in the medium. The MCRT technique consists in computational simulation of that chain and in calculating a statistical estimate for the desired properties of interest (Marchuk et al., 1980), e.g., the radiation regime in the scene and the remote sensing signal received by a sensor. Though there are differences for the two subsystems as mentioned above, the basic principles of the MCRT method as introduced below can be applied for both subsystems to simulate the RT of the coupled system in a coherent manner.

2.2. Atmospheric module

The simulation scene consists of 1-D atmospheric layers with 3-D canopies from land surface as shown in Fig. 1. Characterization of optical properties and light propagation in the atmospheric layers and the radiative coupling with the land surface are discussed in some more detail in the following subsections.

2.2.1. Characterization of the atmosphere for the tracing of photons

The atmosphere is stratified in a number of plane-parallel layers. Denser samplings for bottom than top atmosphere are adopted to accommodate the fact that the atmospheric density is larger for the former. By default, 15 layers were chosen to model the atmosphere module with the height from 0 km to 50 km and top heights of the 15 layers being 1, 2, 3, 4, 5, 6, 7, 8, 9, 10, 12, 16, 20, 30, 50 km, although the number of layers and the height can be changed by the user. The atmosphere is assumed to contain only gases and aerosols, without clouds. Gases and aerosols are characterized by extinction coefficient σ (λ), the single scattering albedo ω (λ), and the phase function P (Θ, λ), where Θ is the scattering angle between Ω' and Ω for the directions of incident and scattered photon, respectively, and λ is the wavelength. MODTRAN (Berk et al., 2000, version 5.2.1) was used to calculate σ (λ) and ω (λ) in each layer for several classical gas and aerosol models. Gas and aerosol phase functions are simulated with the Rayleigh and double Henyey-Greenstein functions, respectively. As in Kobayashi and Iwabuchi (2008), gas and aerosol particles in each atmosphere layer are assumed to form an ensemble with its optical properties calculated by

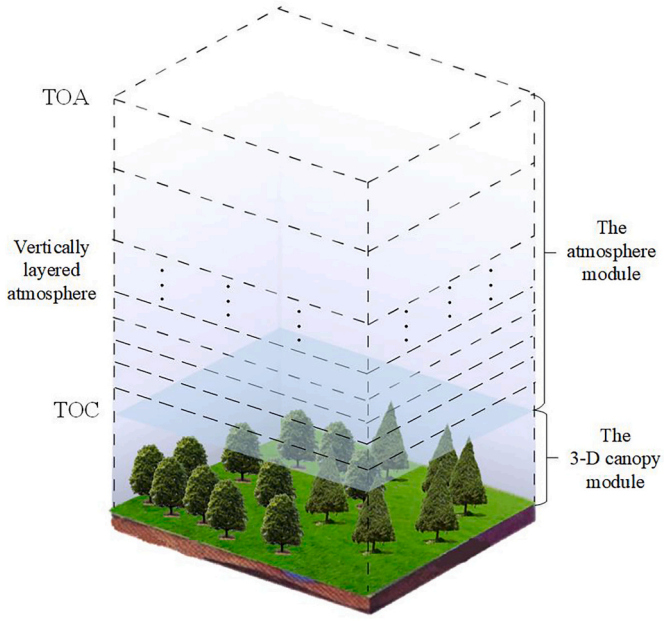

Fig. 1. Schematic representation of the land–atmosphere system.

the weighted average of those from the two components:

$$\sigma_{atm}(\lambda) = \sigma_g(\lambda) + \sigma_a(\lambda) \tag{2}$$

$$\omega_{atm}(\lambda) = \frac{\omega_g(\lambda)\sigma_g(\lambda) + \omega_a(\lambda)\sigma_a(\lambda)}{\sigma_{atm}(\lambda)} \tag{3}$$

$$P_{atm}(\Theta,\lambda) = \frac{\omega_g(\lambda)\sigma_g(\lambda)P_g(\Theta,\lambda) + \omega_a(\lambda)\sigma_a(\lambda)P_a(\Theta,\lambda)}{\omega_g(\lambda)\sigma_g(\lambda) + \omega_a(\lambda)\sigma_a(\lambda)} \tag{4}$$

where the subscripts *atm*, *g*, and *a* represent the atmospheric ensemble, gas, and aerosol, respectively.

With these pre-computed optical properties, we can sample the free length and scattering direction of photons (as explained below) from arbitrary probability density $f(x)$ by computing the cumulative probability density $F(x)$, and inverting it, i.e. the inverse transform sampling (ITS) method:

$$x = F^{-1}(r) \text{ and } F(x) = \int_0^x f(x')dx' \tag{5}$$

where r is a random variable uniformly distributed in [0, 1].

The top plane of the simulation scene is located at TOA, from which photons are launched to simulate light propagation in a physically meaningful way, i.e., in the forward direction with initial direction given by the solar zenith and azimuth angles (θ_s, ϕ_s). Initial flux of a generated photon from the plane is calculated by:

$$Q(\lambda) = \frac{E(\lambda)S\cos\theta_s}{N} \tag{6}$$

where $E(\lambda)$ is the extraterrestrial solar irradiance, S is the plane area, and N is the total number of photons. When a photon enters the scene bounded with a box, the photon's free path length (l_{atm}) until collision takes place is sampled with Eq. (5) by a random number r combined with the exponential probability distribution (Marchuk et al., 1980):

$$l_{atm} = -\frac{ln(r)}{\sigma_{atm,k}(\lambda)} \qquad r \in [0,1] \tag{7}$$

where $\sigma_{atm,\,k}$ is the extinction coefficient of collided ensemble in the kth atmospheric layer, as determined by Eq. (2). At the interaction point, energy of the scattered photon is calculated as:

$$Q_{out}(\lambda) = Q_{in}(\lambda)\omega_{atm}(\lambda) \tag{8}$$

where the subscripts *out* and *in* denote the outgoing and incoming photons, respectively. If the incoming photon carries excited fluorescence flux $Qf_{in}(\lambda)$ in the range of 640–850 nm, the fluorescent flux of the scattered photon is similarly updated: $Qf_{out}(\lambda) = Qf_{in}(\lambda) \bullet \omega_{atm}(\lambda)$.

The outgoing direction of the scattered photon is determined by the ITS method according to Eq. (5). In general scattering direction cannot be solved analytically with the composite phase function $P_{atm}(\Theta, \lambda)$. A look-up table (LUT) is pre-generated to tabulate scattering angle between directions Ω' and Ω for a set of r uniformly distributed in [0, 1]. Azimuth angle of the scattered photon is uniformly sampled in [0, 2π]. The scattering direction is then determined with respect to the local coordinate system and further transformed in the world Cartesian system. The position, energy, and direction of the scattered photon are updated for further collision and scattering calculations.

2.2.2. Energy collection and radiative coupling with the surface

At each collision site, the spread method (noted as "local estimation" in MCRT methods for atmosphere (Marchuk et al., 1980)) is invoked to accumulate energy contributions to the pre-defined detector with viewing direction of Ω_o located at infinity. The non-fluorescent and fluorescent radiance contributions, L_o and Lf_o, are computed as:

$$\begin{aligned} L_o^{atm}(\Omega_o,\lambda) &= \frac{Q_{in}(\lambda)\omega_{atm}(\lambda)P_{atm}(\Theta,\lambda)T_{atm}(\lambda)}{4\pi\cos\theta_o S} \\ Lf_o^{atm}(\Omega_o,\lambda) &= \frac{Qf_{in}(\lambda)\omega_{atm}(\lambda)P_{atm}(\Theta,\lambda)T_{atm}(\lambda)}{4\pi\cos\theta_o S} \end{aligned} \tag{9}$$

where θ_o is the zenith angle of the senor. The scattering phase function for aerosol particles can span several orders of magnitude and result in noisy TOA radiance spectrum if the peaks in the forward directions by $P_{atm}(\Theta, \lambda)$ were not corrected. In actual implementation, the peak truncation method proposed by Iwabuchi (2006) was adopted to improve convergence without introducing bias. T_{atm} is the atmosphere transmittance along the view direction of Ω_o from the collision site to the sensor. In practice, T_{atm} is calculated with Lambert-Beer's law meanwhile by considering the fact that the photon may pass through multiple atmospheric layers:

$$T_{atm}(\lambda) = exp\left[-\sum_{layers} l_{atm,i}\sigma_{atm,i}(\lambda)\right] \tag{10}$$

where $l_{atm,\,i}$ and $\sigma_{atm,\,i}$ are respectively the photon's free path length and the extinction coefficient of collided ensemble in the ith atmospheric layer.

For comparisons with near-surface observations, it is desirable to reproduce as faithfully as possible the actual measurement conditions, such as the detector's distance to the ground and field-of-view (FOV). To allow this, only the contributions coming from the detector's footprint are collected, as detailed in Zhao et al. (2015).

If the photon leaves the simulation scene through the side, the photon re-enters at the opposite side to impose cyclic boundary conditions. We repeat the tracing process in the atmosphere until (1) the photon leaves the scene at TOA; (2) energy of the photon is lower than a predefined threshold and the photon does not survive the Russian roulette (Zhao et al., 2016); or (3) the photon enters the canopy and hits the canopy components (described in the next section). Scattered photons from the canopy to the atmospheric layers similarly follow the above tracing procedures. This consistent simulation of RT in the coupled land–atmosphere system enables accurate treatment of multiple scattering between the vegetation and atmosphere.

2.3. Canopy module

The implementation of the forward ray-tracing method to simulate

RT for the explicit canopy representation is elaborated in Zhao et al. (2015, 2016). By coupling with the atmospheric module introduced above, TOA radiance with SIF can be simulated for relatively small sized explicit canopy scenes (e.g. 0.1 km × 0.1 km). Hyperspectral simulation, including SIF, is feasible yet not practical on a common personal computer for realistic scenes composed of explicit canopies at kilometer-scale by WPS, due to the prohibitive requirements on computer resources. Statistical representation of the canopy structure is ideally suited for the simulation of such large scale scenes. With geometrical primitives composed of turbid medium to describe 3-D canopies, canopy scene is greatly simplified and less computer time and resources are required, yet without the loss of key 3-D structural characteristics.

2.3.1. Characterization of the canopy for tracing of photons

Geometrical primitives (e.g., ellipsoids, cylinders, and cones) defined by their locations and dimensions are generated to represent the crowns before the tracking of photon trajectories. The turbid medium analogy of foliage elements (leaves, stems and branches) is assumed within each crown, and characterized by vegetation statistics, e.g., foliage area density, angular distribution and size, and optical properties, e.g., reflectance, transmittance, and fluorescence emission. The stem is approximated as a cylinder below the crown. Woody materials inside the crown are represented by the scaled primitive as the crown and located at lower part of the crown. Schematic representation of the turbid medium abstraction of canopy structure used in WPS can be found in Section 2 of the Supplementary Data (Fig. S1). In the following, tracing of photons is exemplified by the interactions of the photons with the leaf component for simplicity. The interactions of photons with other components are similar with the replacement of their corresponding properties.

A deterministic ray-object intersection test is performed outside the canopy to find the closest crown along the ray, during which the photon experiences extinction with the Lambert-Beer term $\exp.(-\sigma_{atm}\bullet l_{atm})$. Once the photon enters the crown, the photon's free path length (l_c) between two consecutive collisions is similarly calculated by the ITS method and given by:

$$l_c = -\frac{ln(r)}{G(\Omega_{in})\cdot\mu_L} \qquad r \in [0,1] \tag{11}$$

where G is the so-called G-function defined as the projection of a unit leaf area in the direction of photon travel Ω_{in} (Ross, 1981), and μ_L is leaf area density equivalent to total one-sided leaf area per unit volume (cm^2/cm^3). Even with the assumption of a uniform leaf azimuth distribution, one has to resort to approximations or numerical integrations to calculate G, except for few special types of leaf inclination distribution function (LIDF) (Goel, 1988). We adopt the LIDF proposed by Verhoef (1998) with two parameters to control average leaf inclination angle and LIDF bimodality, which can represent most LIDF types adequately. G-function is then obtained by $G(\Omega_{in}) = k/\cos(\theta_{in})$, in which k is the extinction coefficient for direct sunlight in the SAIL model and calculated for a given LIDF by an analytical method at 13 discrete leaf inclination angles and then weighted integration (Verhoef, 1984).

At the collision site, the zenith angle of leaf normal is chosen at random with the ITS method according to the LIDF, and the azimuth angle of the leaf normal is uniformly sampled in [0, 2π]. Then we add up the contribution of the photon's energy to the detector (i.e. the spread method) with the bi-Lambertian leaf plate scattering model:

$$f_L(\Omega_{in}\rightarrow\Omega_o;\Omega_L,\lambda) = \begin{cases} \pi^{-1}\rho_L(\lambda)|\Omega_L\cdot\Omega_o|, & (\Omega_L\cdot\Omega_o)(\Omega_L\cdot\Omega_{in})\langle 0 \\ \pi^{-1}\tau_L(\lambda)|\Omega_L\cdot\Omega_o|, & (\Omega_L\cdot\Omega_o)(\Omega_L\cdot\Omega_{in})\rangle 0 \end{cases} \tag{12}$$

where ρ_l and τ_l are reflectance and transmittance of the leaf, respectively. The virtually spreading photon will experience attenuation from the collision site to the sensor by the vegetative components and atmospheric medium. The attenuation by atmosphere can be calculated by Eq. (10). Gap fraction $p_o(\Omega_o)$ quantifies the attenuation within the canopy, computed as: $p_o(\Omega_o) = \exp.[-G(\Omega_o)\bullet\mu_L\bullet l_z]$, where l_z is the total effective path length from the site to the top of canopy along Ω_o. If the incoming photon at the collision site comes from direct sunlight, i.e. without being scattered by either atmospheric particle or vegetative component before, a correction function of the hotspot effect is applied:

$$C_{\text{hotspot}} = exp\left[\sqrt{G(\theta_s)l_s G(\theta_o)l_o}\,\mu_l\frac{1-exp(-k_l l_{so})}{k_l l_{so}}\right] \tag{13}$$

where k_l and l_{so} are the hotspot parameter and the vectorial difference between incident solar and viewing path length, respectively, with details given in Zhao et al. (2010). Note that C_{hotspot} equals 1 for second and higher orders of scattering, i.e. no hotspot correction applied. Then the radiance contribution from the leaf is calculated as:

$$L_o^L(\Omega_o,\lambda) = \frac{Q_{in}(\lambda)f_L(\Omega_{in}\rightarrow\Omega_o;\Omega_L,\lambda)p_o(\Omega_o)C_{\text{hotspot}}T_{atm}(\lambda)}{cos\theta_o S} \tag{14}$$

If the collision site is on soil, substitute the soil reflectance correspondingly.

After the collection of photon energy, reflection or transmission from a leaf takes place as follows: A random number r is generated to determine whether the photon is reflected or transmitted. If r is in the range of [0, 0.5], reflection happens with the energy of the reflected photon calculated as $2\bullet Q_{in}(\lambda)\bullet\rho_L(\lambda)$; otherwise the photon is transmitted and the energy of the transmitted photon equals to $2\bullet Q_{in}(\lambda)\bullet\tau_L(\lambda)$. The multiplication by 2 ensures energy conservation of the photon. The direction of reflected (or transmitted) photon is determined using the Lambertian scattering with the directions of the incident photon and the leaf normal chosen earlier. The reflection by the soil follows the same procedures with the replacement of its corresponding reflectance and normal vector. The anisotropy of soil surface can also be considered in WPS, which is simulated by the semiempirical model proposed by Rahman et al. (1993).

2.3.2. Excitation of fluorescent photons

When the photon in the range of excitation wavelengths (400–750 nm) collides with a leaf, fluorescence excitation happens at the collision site. The incoming photon excites fluorescent photons in both backward and forward sides of the leaf. A similar bi-Lambertian leaf emission model to Eq. (12) is used for the collection of fluorescence for excitation and fluorescence wavelengths, λ_e and λ_f, respectively,

$$P_L^f(\Omega_{in}\rightarrow\Omega_o;\Omega_L,\lambda_e,\lambda_f) = \begin{cases} \pi^{-1}\left[M_{b,I}(\lambda_e,\lambda_f) + \phi_f M_{b,II}(\lambda_e,\lambda_f)\right]|\Omega_L\cdot\Omega_o|, & (\Omega_L\cdot\Omega_o)(\Omega_L\cdot\Omega_{in})\langle 0 \\ \pi^{-1}\left[M_{f,I}(\lambda_e,\lambda_f) + \phi_f M_{f,II}(\lambda_e,\lambda_f)\right]|\Omega_L\cdot\Omega_o|, & (\Omega_L\cdot\Omega_o)(\Omega_L\cdot\Omega_{in})\rangle 0 \end{cases} \tag{15}$$

where M is the excitation-fluorescence matrix (EF-matrix) with subscripts "b" and "f" for backward and forward side of the leaf, and "I" and "II" for photosystem I (PSI) and photosystem II (PSII), respectively. These four EF-matrices are obtained from the Fluspect model. φ_f is the correction factor for the fluorescence quantum efficiency for PSII. φ_f is determined by the incident photosynthetic active radiation level (PAR) as proposed by Rosema et al. (1998). In practice, the canopy scene is subdivided into a set of 3-D rectangular cells, or voxels. Every time a

photon collides with the vegetative components within a given voxel, the irradiance contribution over the PAR region (400–700 nm) to the voxel is accumulated. This procedure is implemented ahead of the process of fluorescence excitation to compute incident PAR and then φ_f for each voxel. During fluorescence excitation, φ_f is then retrieved according to the voxel in which the excitation photon is located. The summation of fluorescence over the whole excitation wavelengths with an interval of $\Delta\lambda_i$ nm gives excited SIF collected by a sensor in λ_f,

$$Lf_o^L(\Omega_o,\lambda_f)=\frac{\sum_{\lambda_e=400}^{750} Q_{in}(\lambda_e)P_L^f(\Omega_{in}\rightarrow\Omega_o;\Omega_L,\lambda_e,\lambda_f)\Delta\lambda_i p_o(\Omega_o)C_{\text{hotspot}}T_{atm}(\lambda)}{cos\theta_o S} \tag{16}$$

where the hotspot correction function C_{hotspot} is computed with Eq. (13) for the first-order excitations by direct sunlight. Similarly, C_{hotspot} equals to 1 for second and higher orders of excitations.

After the collection of excited fluorescence, the reflected or transmitted photon continues propagating with excited fluorescent energy. The fluorescent energy of the reflected photon in λ_f equals $2\bullet Q_{in}(\lambda_e)\bullet[M_{b,I}(\lambda_e,\lambda_f)+\varphi_f M_{b,II}(\lambda_e,\lambda_f)]$; and the fluorescent energy of the transmitted photon equals $2\bullet Q_{in}(\lambda_e)\bullet[M_{f,I}(\lambda_e,\lambda_f)+\varphi_f M_{f,II}(\lambda_e,\lambda_f)]$. At the next collision site, the reflected or transmitted photon will contribute to the scattered fluorescence received by the sensor through Eq. (14), and re-excite fluorescence if λ_f is in the range of 400–750 nm.

2.4. Error estimations

MCRT simulations are noisy because a number of photons are randomly traced through the atmosphere and land surface. The radiation we want to compute is the mean of random variables X denoted by $\mu = E[X]$. μ is unbiasedly estimated by generating a sample of photons and calculating the sample mean $<\mu_N>$:

$$\langle\mu_N\rangle=\frac{1}{N}\sum_{i=1}^{N}X_i \tag{17}$$

For a given confidence level p, the error of MC method, ε, can be calculated as (Marchuk et al., 1980):

$$\varepsilon=|E(X)-\langle\mu_N\rangle|\le\frac{z_c\sigma}{\sqrt{N}} \tag{18}$$

where z_c is a constant which depends on the confidence level p. Thus our confidence interval for μ is:

$$\langle\mu_N\rangle\pm\frac{z_c\sigma}{\sqrt{N}}$$

Common choices for p are 95% and 99.7%, for which $z_c \approx 1.96$ and $z_c \approx 3.0$, respectively. σ is the standard deviation of the mean and estimated by its estimator $\hat{\sigma}$:

$$\hat{\sigma}=\sqrt{\frac{1}{N}\sum_{i=1}^{N}X_i^2-\left(\frac{1}{N}\sum_{i=1}^{N}X_i\right)^2} \tag{19}$$

where X_i is the contribution of ith photon to the targeted radiation. Then we can obtain the relative error ε_r under given confidence level and photon numbers:

$$\varepsilon_r=\frac{\varepsilon}{\langle\mu_N\rangle}\times 100\% \tag{20}$$

For the simulation results of WPS in this paper, with the 99.7% confidence level the number of photons was chosen to ensure ε_r was lower than 1% for most of the wavelengths.

3. Material and methods

Two schemes are exploited to evaluate the accuracy of the newly proposed modules in WPS. Firstly, intercomparisons of the WPS model with other RT models based on different formulations under the identical simulation conditions are performed to evaluate the model performance in different aspects of WPS. Specifically, datasets from the exercise of radiation transfer model intercomparison (RAMI) are used to evaluate the simulation of angular distributions of radiation regime by WPS; the newly coupled atmospheric module in WPS is evaluated by comparison with the coupled SCOPE and MODTRAN models for 1-D homogeneous layers of atmosphere and canopy, and the DART model for 1-D homogeneous atmosphere above 3-D heterogeneous canopy. Secondly, evaluations with in-situ measurements consisting of both leaf and canopy data, and spectra collected by an unmanned aerial vehicle system, are performed to test the model under real experimental conditions. For all the WPS simulations, we adopt the new module for canopy representation by geometrical primitives composed of turbid medium (noted as "TM").

3.1. Experiments from the radiative transfer model intercomparison platform to evaluate the 3-D canopy module

A set of experiments from the RAMI Online Model Checker (ROMC, Widlowski et al., 2008) are exploited to evaluate the WPS model. ROMC is an open-access platform to evaluate the accuracy of the canopy RT models by comparison against a reference set, which is generated from an ensemble of 3-D RT models that have been identified as "most appropriate" during the third RAMI phase. Two test canopy scenes in "validate mode" which is suggested by ROMC organizers (Widlowski et al., 2008) are available from the ROMC website. The heterogeneous 3-D canopy scene "HET01_DIS_UNI" in a 100 m × 100 m section, which is more relevant than the horizontally homogeneous 1-D canopy "HOM11_DIS_ERE" for the evaluation of 3-D canopy abstraction, is chosen here to evaluate the WPS model with bidirectional reflectance factor (BRF) and its components, e.g., single scattering and multiple scattering contributions. The description and ROMC results for HOM11_DIS_ERE are provided in Section 3 of the Supplementary Data.

The scene HET01_DIS_UNI contains a large number of non-overlapping spherical objects representing the individual plant crowns with given coordinates of the sphere centers, located over and only partially covering the underlying soil surface. These spherical objects contain randomly distributed finite size disc-shaped scatterers characterized by the specified radiative properties (reflectance and transmittance) in red and NIR bands, and the orientation of the normals to the scatterers following a uniform distribution function. Table 1 summarizes the key structural and spectral information of the canopy scene. The only unknown is the hotspot parameter k_l used in Eq. (13) to consider the hotspot effect. Based on the radius of leaf disk and canopy height, k_l was estimated and further tuned to be 8.5 according to BRF's agreement around the hotspot directions in the red band (Zhao et al., 2010). Detailed introductions with rendered scenes are provided in Section 3 of the Supplementary Data.

Required measurements for model evaluation including total BRFs and their components were simulated by WPS for four scenarios: red

Table 1
Structural and optical properties of the canopy scene.

Leaf Area Index of individual sphere	5.0 [m^2/m^2]
Leaf Inclination Distribution Function	Uniform
Number of spheres	15
Fractional coverage of spheres	0.471
Sphere radius	10.0 [m]
Leaf reflectance (Lambertian)	0.4957 (NIR), 0.0546 (Red)
Leaf transmittance (Lambertian)	0.4409 (NIR), 0.0149 (Red)
Soil reflectance (Lambertian)	0.159 (NIR), 0.127 (Red)

band with sun zenith angle (SZA) of 0°, NIR band with SZA of 0°, NIR band with SZA of 30° and NIR band with SZA of 60°. Measurements were simulated at 2° intervals of viewing zenith angle (VZA) covering the range from −75° (backward) to 75° (forward) in the orthogonal plane (OP). Therefore BRFs for a total of 76 viewing directions were computed. We implemented the simulations according to the ROMC requirement, and submitted our results on-line. The results computed by WPS were then compared against the reference values. The evaluation results include data plots showing grey-coloured envelopes corresponding to 1, 2.5 and 5% of the reference solution, 1 to 1 plots of simulated and reference data, and other statistical results. Here only the most informative evaluation results of data plots for the total BRFs are presented. The comparisons for their components and other evaluation metrics are provided in Section 3 of the Supplementary Data.

3.2. Datasets to compare with the coupled SCOPE and MODTRAN radiative transfer models

Based on the four-stream RT theory, the SCOPE (or its precursor SAIL) and MODTRAN models were coupled to simulate upward non-fluorescent radiance and SIF at TOA (Cogliati et al., 2015; Verhoef and Bach, 2007, 2012; Verhoef et al., 2018). The modeling of the canopy-atmosphere directional effects within the four-stream framework was realized by considering the four reflectance terms of the canopy and their coupling with the atmospheric functions. The coupled SCOPE (v1.73) and MODTRAN (v5.2) models represent the state-of-art scheme to depict the RT interactions of the Earth's surface-atmosphere system for horizontally continuous medium.

To evaluate the WPS model by the coupled four-stream model, the input atmospheric conditions of them are kept as identical as possible, corresponding to the settings in MODTRAN as: a) Gases model: US standard 1976; b) Aerosol model: Rural, with the visibility of 23 km; c) CO_2 mixing rate: 390 ppmv; d) Vertical water vapor column: 1.41 g/cm^2. SZA = 40° and sun azimuth angle (SAA) = 40°. Two homogeneous canopy scenes composed of disc-shaped scatterers with a radius of 2.5 cm with LAI of 1 and 3, with a spherical LIDF, were generated for the comparison. By referring to the ratio of leaf size to the canopy height and the agreement of BRFs in red bands between WPS and the SCOPE model, the semiempirical hotspot parameter s_l in SCOPE was estimated as 0.05 for the two canopies. Correspondingly, the hotspot parameter k_l in WPS was estimated as 12. The following values for the Fluspect (van der Tol et al., 2019) input parameters in SCOPE were used: leaf chlorophyll = 40 μg/cm^2, carotenoids = 10 μg/cm^2, leaf equivalent water thickness = 0.02 cm, dry matter content = 0.005 g/cm^2, mesophyll structural parameter N = 1.5, and fluorescence quantum efficiencies for PSI and PSII are 0.002 and 0.01, respectively. The soil reflectance spectrum in SCOPE with 5% volume moisture content was used. Lambertian scattering by leaf and soil is assumed in both models. Since the correction factor for the fluorescence quantum efficiency of PSII is calculated differently in the SCOPE and WPS models, it is fixed as 1 in both models to reduce the uncertainties.

Spectral simulations at nadir are performed and compared at the 0.15 nm and 1 nm resolutions in the range of 400–850 nm (640–850 nm for SIF). Besides the same final output of the TOA radiance (L_{TOA}), the TOC radiance (L_{TOC}) and TOA SIF (F_{TOA}), the direct comparisons of the following simulations are feasible and also provided in the next section or the companioning Supplementary Data (Section 4):

a) atmospheric transmittance, including direct atmospheric transmittance for solar radiation (τ_{ss}), diffuse atmospheric transmittance for solar radiation (τ_{sd}), and total atmospheric transmittance for solar radiation (τ_{tot}) at the ground level;
b) atmospheric path radiation (Path), which is the contribution scattered by the atmosphere into the viewing direction without interaction with the ground;
c) the bi-directional radiance by the target (L_{so}), which is the sunlight reflected by the target and transmitted directly to the sensor;
d) SIF observed at TOC, F_{TOC}, and emitted SIF transmitted directly to the sensor at TOA, F_{em};

To evaluate the performance of multi-angular simulations of radiance and SIF at TOC and TOA by WPS, the simulations for the 1 nm resolution in the principal plane (PP, viewing azimuth angle aligned with solar azimuth angle) and OP, at the positions of the red and far-red peaks (685 nm and 740 nm), are compared with VZAs varying from −60° to 60° with a step of 5°. The angular region near the hotspot directions is over sampled using a step of 1° in the range of 34° and 46°. Accordingly, the statistical results for the simulations by both models for a total of 60 viewing angles (35 in PP and 25 in OP) at the two wavelengths are provided.

3.3. Datasets to compare with the DART model

The DART model can simulate the SIF signal of 3-D canopies observed by sensors at both TOC and TOA. Here a scenario of horizontally continuous atmosphere on top of discrete 3-D canopies was designed to compare the simulated results by WPS and the DART model. The input atmospheric conditions corresponds to the settings in MODTRAN as: a) Gases model: US standard 1976; b) Aerosol model: Rural, with the visibility of 23 km; c) CO_2 mixing rate: 400 ppmv; d) Vertical water vapor column: 1.41 g/cm^2. SZA = 30° and SAA = 225°. The generated forest scene (20 m × 20 m × 6 m) used for WPS is composed of 21 ellipsoidal crowns with the same dimension of 2.0 m × 2.0 m × 3.0 m for three semi-axes. The tree crowns have the same LAI of 3.0 with uniform LIDF, constructed with 1200 leaf disks with a radius of 10 cm. The hotspot parameter k_l in WPS was estimated as 2. Accordingly, the information of the exact locations and dimensions of the trees and the tree structure was imported in DART to generate the 3-D arrays of voxels containing turbid medium (statistically characterized by LAI and LIDF). Then DART simulations (v5.7.9) were carried out to simulate radiance and SIF spectra with the flux tracking algorithm using some of the following key settings: 100 discrete directions to divide the 4π space (Yin et al., 2013), cyclic boundary conditions to emulate an infinite scenario, total thickness of mid atmosphere equal to 4000 m with thickness of each layer within being 1000 m, total thickness of high atmosphere equal to 52,000 m with thickness of each layer within being 2000 m, the hotspot parameter estimated as 0.06, and Lambertian scattering by leaf and soil. Default values or options of other settings in DART were chosen for the simulations. The following values for the Fluspect input parameters were used: leaf chlorophyll = 30 μg/cm^2, carotenoids = 10 μg/cm^2, leaf equivalent water thickness = 0.012 cm, dry matter content = 0.0017 g/cm^2, mesophyll structural parameter N = 1.8, and fluorescence quantum efficiencies for PSI and PSII are 0.002 and 0.01, respectively. The correction factor for the fluorescence quantum efficiency for PSII is fixed as 1 in both the DART and WPS models. More information about the forest scene, including graphical representation, can be found in Section 5 of the Supplementary Data.

The excessive computer memory and simulation time required by DART flux tracking (elaborated in the Discussion section) prohibit the comparison for a spectral resolution of 0.15 nm in the range of 400–850 nm. In the following, simulations of the TOA radiance (L_{TOA}) and SIF at nadir with two resolutions of 0.5 nm and 1 nm are compared. Besides, the intermediate outputs by DART, e.g., atmospheric path radiation and SIF observed at TOC, are also compared with those by the WPS model. For the comparisons of multi-angular radiance and SIF at TOC and TOA in the PP and OP by both models, simulations at 685 nm and 740 nm are performed for the 1 nm resolution with VZAs ranging from −60° to 60° with a step of 5°. The angular region near the hotspot directions is over sampled using a step of 1° in the range of 24° and 36°. Accordingly, the statistical results for the simulations by both models for a total of 60 viewing angles (35 in PP and 25 in OP) at the two wavelengths are provided.

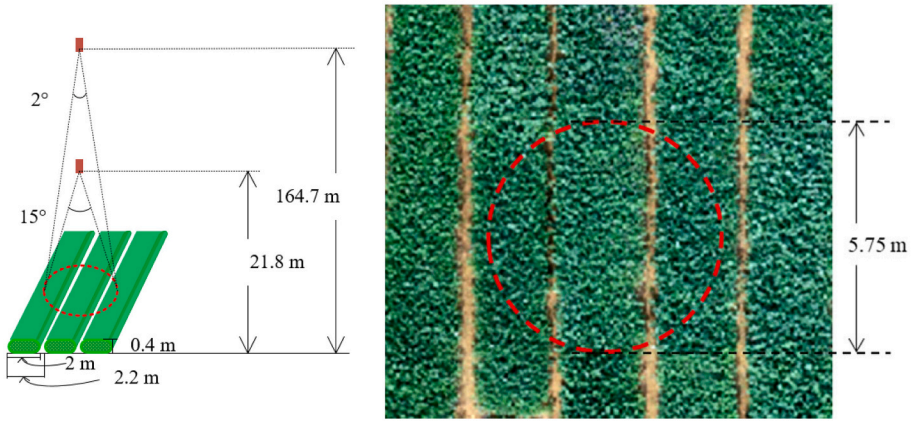

Fig. 2. Scheme of rapeseed canopy spectrum measurements. (a) Two flights with different combinations of spectrometer field of view and altitude above ground level: (15°, 21.8 m) and (2°, 164.7 m); (b) Photon taken by the onboard camera with the red circle showing the footprint of the spectrometer for two flights. (For interpretation of the references to colour in this figure legend, the reader is referred to the web version of this article.)

3.4. Experimental datasets for model evaluation

The field experiment was carried out at a test site inside Huazhong Agricultural University (30.47° N, 114.35° E), Wuhan, China, on 13 December 2019. The site is characterized by a sub-humid continental monsoon climate with mean annual temperature and rainfall of 16.7 °C and 1205 mm, respectively. Rapeseed (cultivar Zhongshuang 11) was sown in north-south direction on 30 September 2019 with row spacing of 2.2 m. Row structural parameters are shown in Fig. 2. Three kinds of data used in this study are as follows.

a) Canopy hyperspectral measurements through unmanned aerial vehicle

A QE Pro spectrometer (Ocean Optics, Dunedin, Florida, USA) was mounted on an unmanned aerial vehicle (UAV) system composed of DJI Matrice 600 Pro (DJI, Shenzhen, China), a red-green-blue (RGB) camera and real time kinematic (RTK) to collect the spectra of rapeseed canopy at nadir direction. The spectrometer is equipped with a back-thinned CCD detector, a 25 μm entrance slit, a long-pass filter (>590 nm), and a H6 grating to cover the spectral range of 650–808 nm with spectral resolution of 0.31 nm, spectral sampling interval of 0.15 nm, and signal-noise-ratio (SNR) of 1000. Two flights with different combinations of spectrometer FOV and altitude above ground level (AGL), (15°, 21.8 m) and (2°, 164.7 m), were conducted by trying to keep their footprints on the ground unchanged with the assistance of the RGB camera and RTK. The red circle shown in Fig. 2b delineates the targeted footprint with a diameter of 5.75 m encompassing more than two rows in the cross row direction, which can ensure that representative canopies were sampled (Zhao et al., 2015).

UAV-based canopy spectrum measurements were conducted under clear sky and light wind (< 3.5 km/h) conditions during 13:00–14:00 local time. Before each flight, solar direct and skylight irradiances were measured with the calibration panel over the ground. Then the UAV flew above the targeted canopy to take the spectral measurements. Through the real-time transferred video taken by the RGB camera onboard UAV, the footprint by the spectrometer can be shown in the image thanks to the geo-calibrated camera and spectrometer's fiber optic. By fine-tuning the UAV location, the spectra of the targeted footprint can be measured. Five measurements were taken and averaged to output the mean spectrum.

b) Leaf and canopy measurements in the field

Concurrent with each UAV flight measurement, spectral properties of three leaves at different heights in the neighboring rapeseed rows, including reflectance, transmittance, and fluorescence for backward and forward directions, were measured by FluoWat (van Wittenberghe et al., 2013) coupled with the RS-8800 spectrometer (Spectral Evolution, Massachusetts, USA). The spectrometer covers the spectral range of 350–1000 nm with a resolution of 2.8 nm, a spectral sampling interval of 1 nm, and SNR > 1500. By following the measurement sequence of the FluoWat leaf clip (https://doi.org/10.17026/dans-xym-hhbq) suggested by van der Tol et al. (2019), transmittance, reflectance, and fluorescence of the leaves were measured. With these spectra, a two-stage inversion of the Fluspect model as described in Zhao et al. (2016) was performed to obtain the four EF-matrices used by the WPS model (Eq. (15)). The reflectance spectra of the bare soil close to the targeted canopy were also measured with RS-8800 at the height of ~1 m above the ground with a 10° FOV fiber optic adapter in nadir viewing direction.

After the UAV-based spectral measurements, average values of the LAI and average leaf inclination angle of the targeted canopy were measured near dusk with LAI-2200 (LI-COR, Lincoln, Nebraska, USA) as being 5.8 and 31.7°, respectively, by following the instruction manual (LI-COR Inc, 2012, https://www.licor.com/documents/6n3conpja6uj9aq1ruyn). Combined with the row structural measurements as shown in Fig. 2a, the rapeseed scene was generated for WPS simulations with the hotspot parameter k_l estimated as 2.

c) Measurements of the atmospheric conditions

A sun tracking photometer CE318 (Cimel Electronique, Paris, France) installed on the campus of Wuhan University with a direct distance of 6.9 km from the experimental site continuously recorded the atmospheric transmissivity during the flight campaign. Aerosol parameters, e.g. aerosol optical depth (AOD) at 8 wavelengths (340, 380, 440, 500, 675, 870, 937, 1020, 1640 nm), were retrieved with the algorithm by Dubovik and King (2000). According to the relationship between wavelength and AOD established by Ångström (1964), AOD at 550 nm was determined and used to calculate the atmospheric visibility as 13.6 km. The atmospheric profile (mid-latitude winter) and aerosol type (urban) were determined by the time and location of the experiment. The measured direct solar irradiance and skylight irradiance which can also be simulated by the WPS model were used as constraining conditions to adjust the values for the atmospheric visibility and water vapor column. Then the following atmospheric parameters corresponding to the settings in MODTRAN were used to obtain the layered atmospheric parameters in WPS: a) Gases model: mid-latitude winter; b) Aerosol model: urban, with the visibility of 15.5 km; c) CO_2 mixing rate: 400 ppmv; d) Vertical water vapor column: 0.85 g/cm^2. VZA = 0°, SZA = 58.07°/59.05° and SAA =205.8°/208.3° for the AGL altitude of 21.8 m/164.7 m.

With the obtained leaf, canopy and atmospheric parameters, the WPS model was used to upscale the SIF signal from leaf to above the canopy at different AGL altitudes with corresponding FOVs. Both SIF and total radiance at different AGL altitudes can be simulated by WPS. But retrieval of the SIF signal from total radiance of UAV measurements needs more concurrent measurements (explained in the Discussion section) which we did not carry out. So only the simulated total radiance spectra are compared with the measured ones.

3.5. Accuracy assessment

The coefficient of determination (R^2) and root-mean-square error (RMSE) were used to evaluate the performance of the WPS model. Besides, the average absolute relative error (AARE) calculated by Eq. (21) was also applied to quantify the relative difference of various quantities simulated by WPS and the reference values, which are either simulated by other RT models, or experimental datasets:

$$\mathrm{AARE} = \frac{\sum_{i=1}^{n}\left|\frac{X_{\mathrm{WPS},i}-X_{\mathrm{ref},i}}{X_{\mathrm{ref},i}}\right|}{n}\times 100\% \quad (21)$$

where $X_{\mathrm{WPS},\,i}$ and $X_{\mathrm{ref},\,i}$ are the quantity simulated by WPS and used for reference at ith wavelength, respectively.

A number of model comparison metrics are provided when assessing the WPS model via ROMC, including graphs of direct BRF comparison plots and some specifically designed statistical indicators. Explanations and results of these statistical indicators are presented in Section 3 of the Supplementary Data.

4. Model evaluation

4.1. Evaluation of the 3-D canopy module via the RAMI online model checker

Comparisons of BRF distributions simulated by WPS for canopy HET01_DIS_UNI with the "surrogate truth" solutions (noted as "ROMCREF") in the OP are shown in Fig. 3. For a SZA of 0° (Fig. 3a-b), the hotspot effect is evidently present and it can be accurately simulated by WPS according to the agreements with reference solutions around the hotspot directions. Three grey-coloured envelopes corresponding to 1, 2.5 and 5% of the BRF of the "surrogate truth" solution surround the

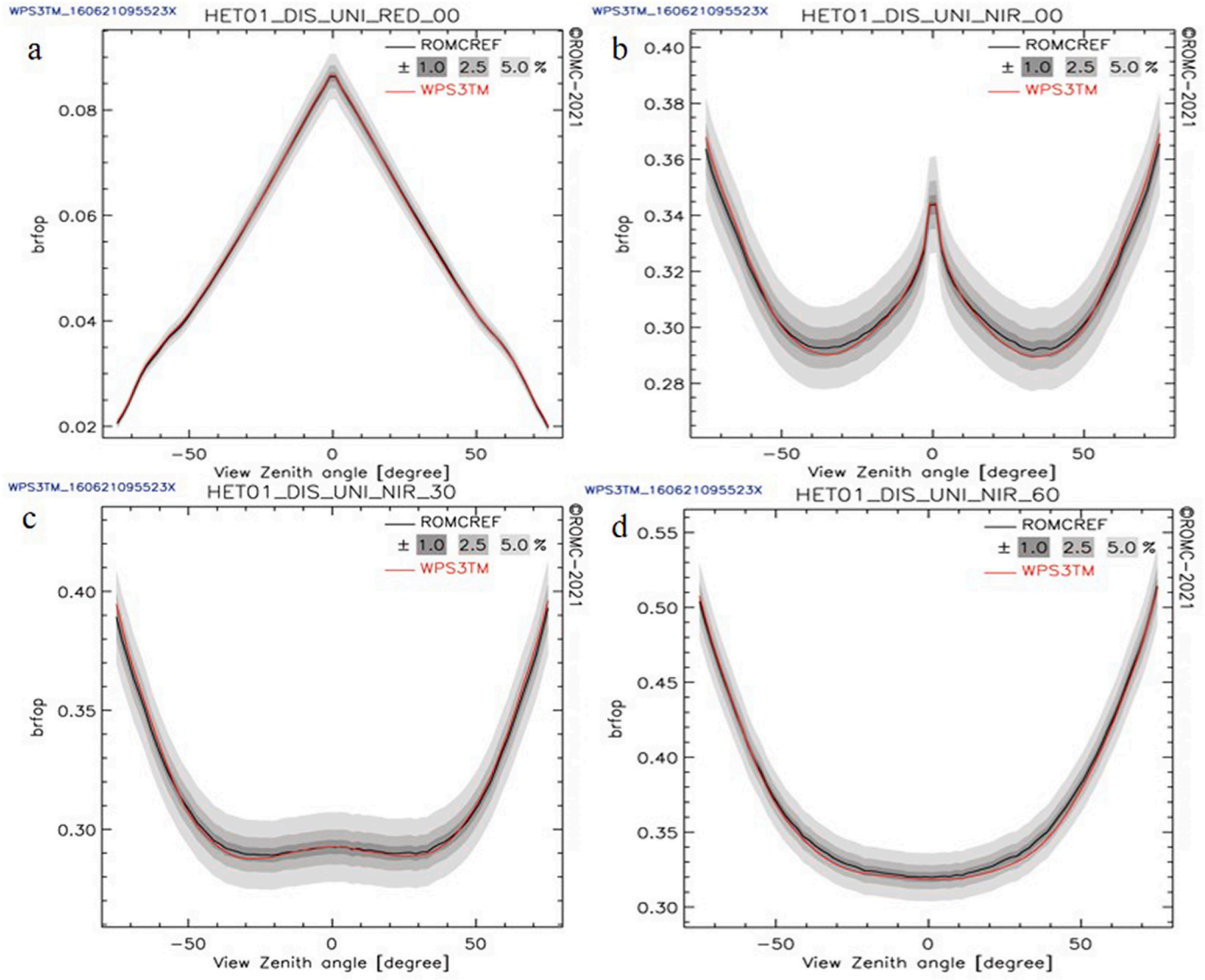

Fig. 3. Comparisons of BRF distributions simulated by WPS (version 3 with the turbid medium module, thus noted as "WPS3TM") with the "surrogate truth" solutions (noted as "ROMCREF") in the orthogonal plane. a: BRF in red band for sun zenith angle of 0°; b-d: BRF in NIR band for sun zenith angle of 0°, 30°, and 60°, respectively. (For interpretation of the references to colour in this figure legend, the reader is referred to the web version of this article.)

reference solution. From these data plots we can see clearly that all BRFs computed by WPS are in 1% of the "surrogate truth" solution. The comparisons of total BRFs combined with comparisons of BRFs' components and other evaluation metrics for the two canopy scenes shown in Section 3 of the Supplementary Data demonstrate that the newly developed module in WPS, i.e. RT simulations for the turbid canopy representation, has the ability to truthfully reproduce the angular distributions of BRF for a 3-D heterogeneous canopy.

4.2. Comparison with the coupled SCOPE and MODTRAN models

Here we present the comparisons of the spectral radiance and SIF distributions at both 0.15 nm and 1 nm resolutions in the range of 400–850 nm (640–850 nm for SIF), the directional radiance and SIF at TOA, and the statistical results. Limited by space, the comparisons of atmospheric transmittance, path radiation, and the directional radiance and SIF at TOC are provided in Section 4 of the companioning Supplementary Data.

The spectra of TOA radiance (L_{TOA}) and its components: bi-directional radiance by the canopy (L_{so}) at nadir simulated by WPS and the SCOPE and MODTRAN models for two canopies are shown in Fig. 4. The spectra of L_{TOA} simulated by both models show the characteristic spectral distribution of green vegetation: strong absorption by leaves in red regions, radiance plateau in NIR regions because of high reflectance and transmittance of leaves, and various absorption lines (more evident for 0.15 nm resolution, Fig. 4a and c) caused by gases. The radiance spectra simulated by WPS and the SCOPE and MODTRAN models agree quite well in both general shapes and local details (insets of the figures) for two canopies. With the increase of LAI, the agreements of radiance spectra for both spectral resolutions improve (Fig. 4c and d).

Simulated SIF signals for TOC and TOA observations by the two models are compared in Fig. 5. At TOC the SIF spectra is smooth without the absorption of telluric gases. However, the spectral smoothness is partly lost for observations at TOA most evidently around absorption bands by O_2-A (centered at 760.4 nm), O_2—B (687.0 nm) and water vapor (714–722 nm). Generally SIF spectra at both TOC and TOA simulated by WPS and the SCOPE and MODTRAN models are very close with each other. Noticeable deviations appear mainly in the atmospheric absorption bands and abate with the increase of LAI. The comparisons of SIF components between these models show that the deviations mainly come from the scattering contributions inside the canopy and later interaction with the atmosphere because the emitted SIF transmitted directly to the sensor at TOA, F_{em}, agrees very closely with each other. The four-stream theory and the discrete ordinate algorithm (with 8 streams here) are adopted in SCOPE and MODTRAN, respectively, to simulate the RT in the coupled canopy and atmosphere. Nevertheless, the WPS model is based on a ray-by-ray tracing manner with which any scattering direction is possible by following the assumed scattering laws. Besides, parameterization methods are also quite different for these models. As a result, these differences can explain the deviations of the simulations.

Fig. 6 shows the comparison of TOA radiance and SIF at 685 nm and 740 nm along the PP and OP simulated by WPS and the coupled SCOPE and MODTRAN models. The hotspot effect is evident for both total radiance and SIF along PP due to the finite size of vegetative scatterers. The agreements around the hotspot directions for TOA total radiance are better than those for TOA SIF because the estimated hotspot parameter s_l in SCOPE is partly based on the agreement of BRFs between these two

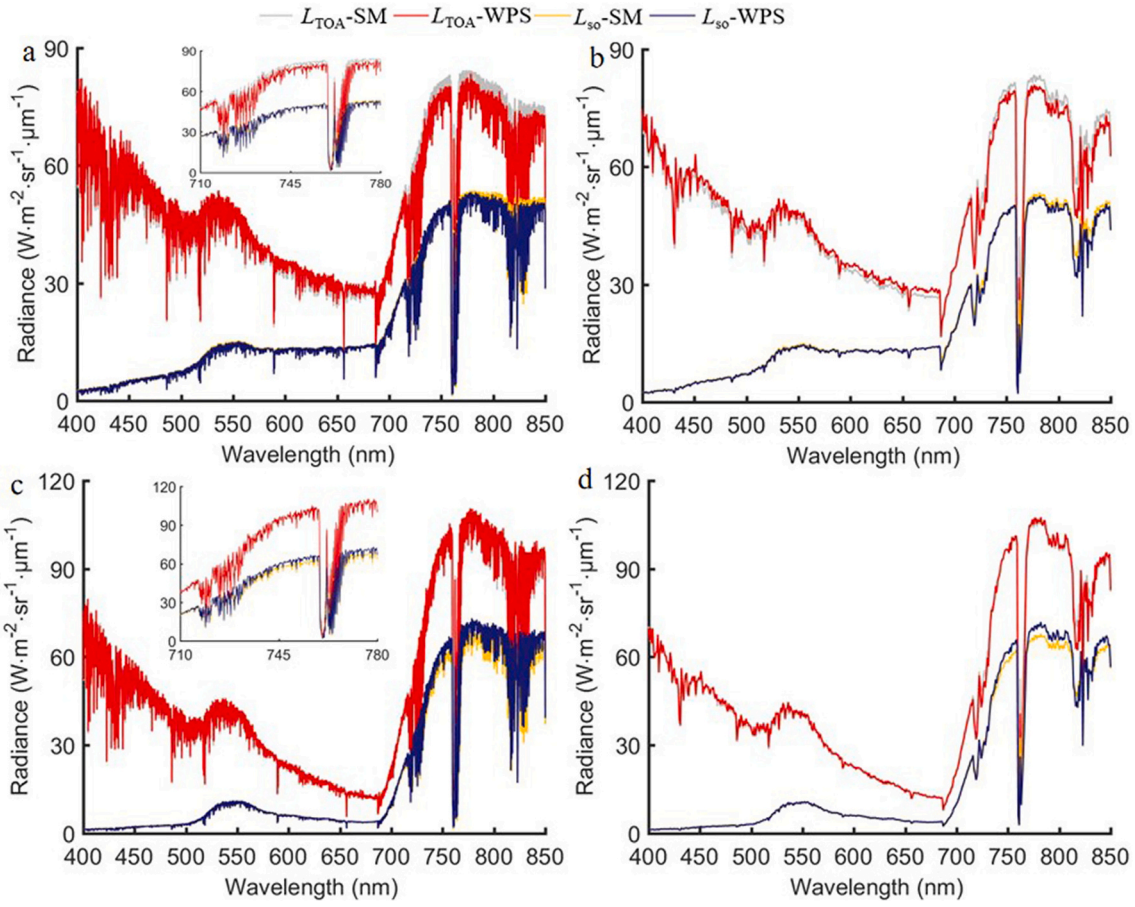

Fig. 4. Spectral distributions of TOA total radiance (L_{TOA}) and bi-directional radiance (L_{so}) simulated by WPS and the SCOPE and MODTRAN models (noted as 'SM') for the canopies with LAI of 1 (a and b, first row) and 3 (c and d, second row) at 0.15 nm (a and c, left column) and 1 nm (b and d, right column) resolutions.

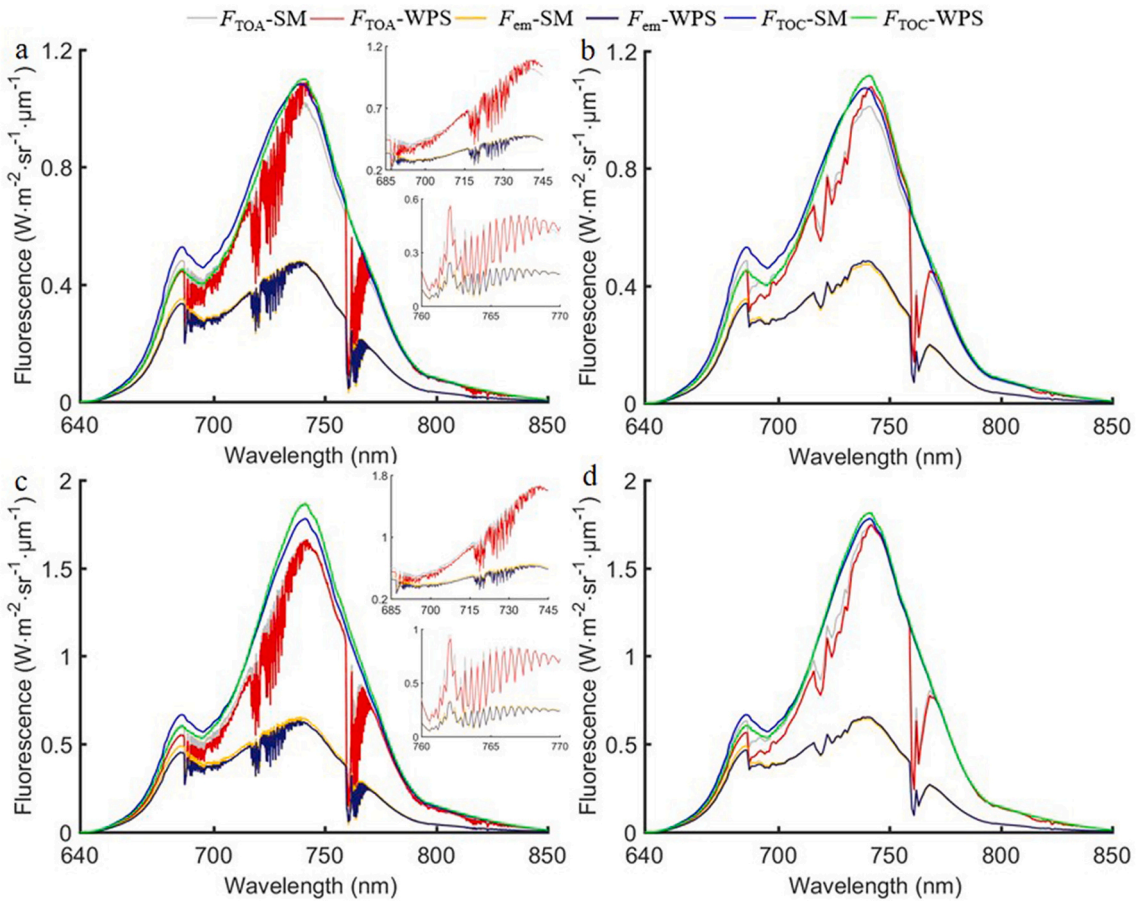

Fig. 5. Spectral distributions of TOC SIF (F_{TOC}) and TOA total SIF (F_{TOA}) and emitted SIF (F_{em}) simulated by WPS and the SCOPE and MODTRAN models (noted as 'SM') for the homogeneous canopies with LAI of 1 (a and b, first row) and 3 (c and d, second row) at 0.15 nm (a and c, left column) and 1 nm (b and d, right column) resolutions.

models. Generally noticeable deviations appear at high VZAs, especially for TOA SIF (Fig. 6c and d) in the backward direction of PP, which can be attributed to the different mechanisms of the models as explained above. Along OP, the shapes of TOA radiance and SIF distributions simulated by WPS accord with those by the SCOPE and MODTRAN models, though radiance simulated at 740 nm by WPS is systematically lower. By checking the corresponding comparisons at TOC (Section 4 in the Supplementary Data), the deviation mainly comes from the radiative coupling between vegetation and atmosphere and later transfer to the TOA sensor. Interestingly, this deviation weakens for SIF, especially high LAI (Fig. 6d).

The statistics of the models' fitting results are provided in Table 2. As noted in the figures, the accordance between the models improves with the increase of LAI. The high R^2 and low RMSE and AARE of all the simulated quantities for two scenarios at two spectral resolutions and multi-angular radiance and SIF in PP and OP at two wavelengths indicate the close agreement between WPS and the coupled SCOPE and MODTRAN models.

4.3. Comparison with the DART model

Fig. 7 presents the comparisons of the spectral path radiation and TOA radiance (first row), and SIF distributions at TOC and TOA (second row) with resolutions of 0.5 nm (left column) and 1 nm (right column) simulated at nadir by two models. It can be seen that both models can simulate the typical spectral distribution of path radiance and TOA radiance for vegetation, and the agreements between two models' simulations are quite good. TOC SIF distributions simulated by two models agree closely, except for the far-red peaks. SIF spectra at TOA simulated by two models show some differences at regions with absorption lines by O_2-A, O_2—B and water vapor. Since TOC SIF simulated by two models agrees very closely with each other in most part of the spectral regions, including the absorption bands, the deviation should be mainly caused by the RT modeling in the atmosphere. Although the optical properties of gas and aerosol used in the two models are both calculated via MODTRAN, the geometry of the atmosphere is represented differently in these two models. In DART the atmosphere is made of 3 regions: bottom, mid and high atmosphere, by which is further divided into a given number of layers with equal thickness (Grau and Gastellu-Etchegorry, 2013). Nevertheless, uneven thicknesses of atmospheric layers are adopted in WPS with smaller thickness for bottom atmosphere. Though we tried to keep the division of the atmosphere as consistent as possible by using more layers in DART and then converting their optical properties to the effective ones for WPS, differences and uncertainties still exist. Besides, the atmosphere RT module in DART uses the discrete ordinate method with the flux tracking approach, different from the ray-tracing method by WPS. Therefore, the different formulations of the two models contribute to the deviations noticed above.

Fig. 8 shows the comparison of TOA radiance and SIF at 685 nm and 740 nm along the PP and OP simulated by WPS and the DART model. Generally the shapes of TOA radiance and SIF distributions simulated by two models agree closely. Notable deviations appear at high VZAs in the backward direction for TOA radiance at 740 nm which can be explained by the different formulations of the two models. However, this deviation weakens for TOA SIF at 740 nm. Similar good agreements are also achieved for the angular distributions of TOC total radiance and SIF (Section 5 in the Supplementary Data). The good accordance at both

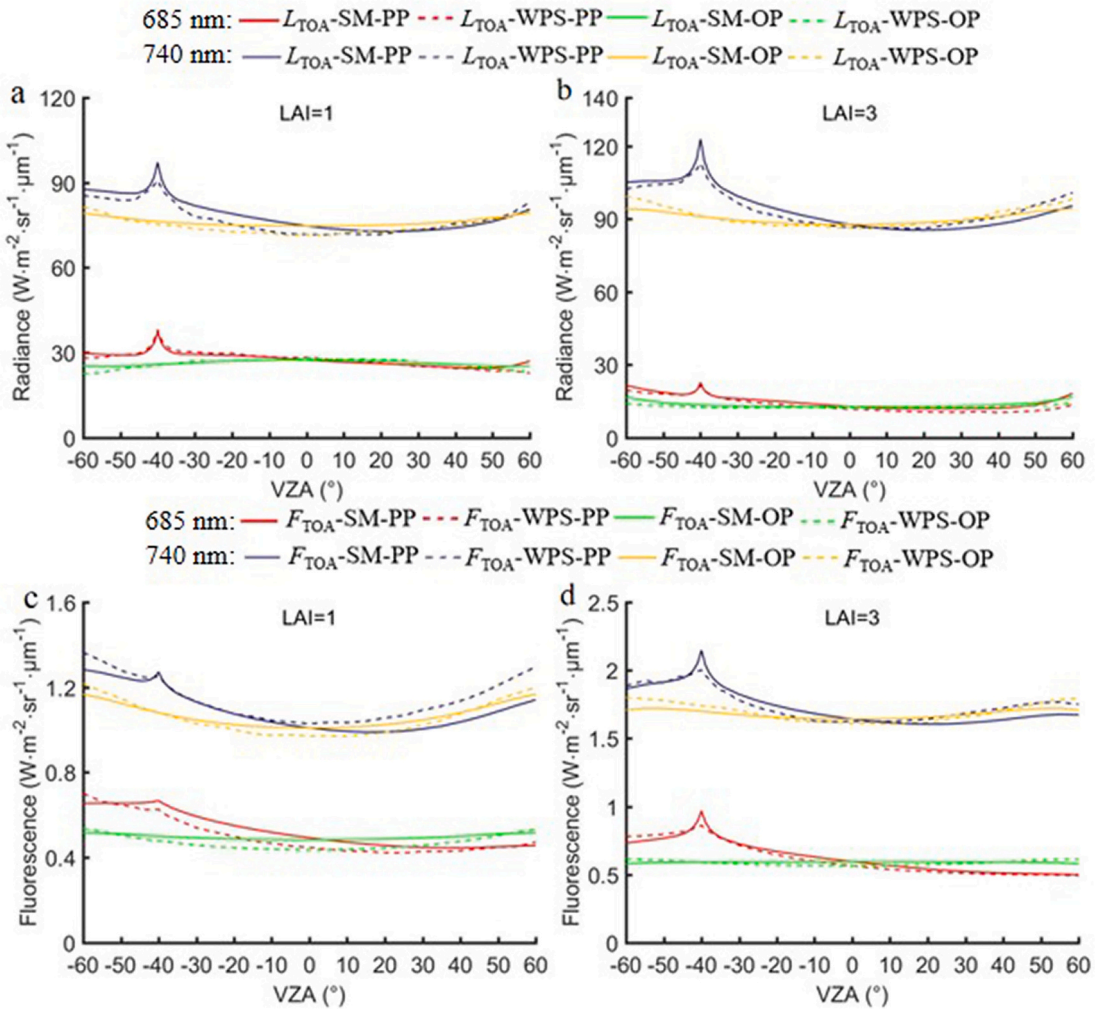

Fig. 6. Angular distributions of TOA total radiance (L_{TOA}, a and b, first row) and SIF (F_{TOA}, c and d, second row) at 685 nm and 740 nm along the solar principal plane (PP) and orthogonal plane (OP) simulated by WPS (dashed line) and the SCOPE and MODTRAN models (noted as 'SM', solid line) for the canopies with LAI of 1 (a and c, left column) and 3 (b and d, right column).

TOC and TOA levels enhances the confidence of the radiative coupling between vegetation and atmosphere simulated in both models.

Table 3 gives the statistics of the models' fitting results. The generally good agreement as shown in the figures between two models is confirmed with the high R^2 and low RMSE and AARE of the simulated quantities.

4.4. Comparison with in-situ measurements

Fig. 9 presents the comparisons of radiance spectra at two AGL altitudes measured by the UAV system and simulated by WPS. The values and general shapes of simulated radiance spectra with two AGL altitudes agree fairly well with those by the measured ones. Noticeable differences are mainly found in the red regions for spectra with the AGL altitude of 164.7 m, which can be explained by the limitation of experimental setups. To ensure the measurement of radiance spectra by UAV and spectral properties of leaf samples and soil on the ground as concurrent as possible, the targeted footprint was chosen with the consideration of easy access, which is located at the east and south corner of the plot. As a result, the distances of the center of the footprint to the east and south soil roads are around 7 m. When the height of UAV reaches 164.7 m, it is likely that contributions reflected from the soil can reach sensor's FOV and introduce differences mainly appeared in red regions due to strong contrast of spectral properties between soil and leaf. Other factors that can introduce the deviations include the neglect of clumping effect of leaves during the generation of canopy scenes and variable SNR values of the spectrometer in field conditions (Marrs et al., 2021). Other major differences for both AGL altitudes in the range of 795–805 nm are hard to explain and need further investigation. R^2, RMSE, and AARE between the simulated and measured values are 0.994, 3.845 W·m^{-2}·sr^{-1}·μm^{-1}, and 9.038%, 0.995, 4.295 W·m^{-2}·sr^{-1}·μm^{-1}, and 15.212% for AGL altitudes of 21.8 m and 164.7 m, respectively.

5. Discussion

By capitalizing on recent achievements of the RAMI exercises, we evaluated the capability of WPS with new module of 3-D structure representation to reproduce the angular distribution of the 3-D canopy's BRF. Results show that both BRFs and their components computed by WPS are in 1% of the reference solution, which is the highest accuracy level achievable for an evaluation model through ROMC. Although the simulation of SIF is not included in the reference datasets of ROMC, it can be seen from Eq. (1) that the RT of excited fluorescence within the canopy is essentially the same as that for solar radiation. Besides, with sufficiently strong consensus reached by the canopy RT community after three phases of RAMI exercise, valuable reference datasets via ROMC provide unambiguous proof of the performance of a RT model. Therefore, the new module of 3-D structure representation in WPS is evaluated

Table 2
Statistical results of correlation between WPS and the coupled SCOPE and MODTRAN models for two homogeneous scenes.

Statistical indicators		LAI = 1	LAI = 3
L_{TOA} (TOA, at nadir)	R^2	0.990 [a]	0.998
		0.981 [b]	0.995
	RMSE	2.196	1.502
		2.609	1.979
	AARE	3.636%	2.148%
		4.461%	2.240%
L_{so} (TOA, at nadir)	R^2	0.998	0.999
		0.996	0.997
	RMSE	0.826	1.702
		1.245	1.610
	AARE	0.116%	0.199%
		2.859%	3.240%
F_{TOA} (TOA, at nadir)	R^2	0.992	0.997
		0.992	0.996
	RMSE	0.030	0.035
		0.029	0.042
	AARE	6.386%	4.479%
		5.471%	4.615%
F_{em} (TOA, at nadir)	R^2	0.999	0.999
		0.999	0.999
	RMSE	0.007	0.016
		0.006	0.008
	AARE	2.914%	5.282%
		2.871%	2.579%
L_{TOA} (TOA, in PP and OP)	R^2	0.914 [c]	0.902
		0.918 [d]	0.917
	RMSE	1.050	1.325
		2.297	2.716
	AARE	2.691%	6.938%
		2.494%	2.195%
F_{TOA} (TOA, in PP and OP)	R^2	0.919	0.954
		0.811	0.865
	RMSE	0.036	0.027
		0.049	0.051
	AARE	6.070%	3.237%
		3.164%	2.427%

[a] Values of the statistical indicators at 0.15 nm resolution;
[b] Values of the statistical indicators at 1 nm resolution;
[c] Values of the statistical indicators at 685 nm;
[d] Values of the statistical indicators at 740 nm;

via ROMC. However, since only one heterogeneous canopy scene (i.e. HET01_DIS_UNI) is currently available in validate mode, use of the ROMC with limited test cases should be seen as a first step towards the full participation in a next phase of RAMI, as cautioned by Widlowski et al. (2008). The newest phase (RAMI-V) including various abstract and actual vegetation canopies started in October 2020. We are performing the required simulations by RAMI-V with the extended WPS module. Hopefully more comprehensive evaluation results for WPS through RAMI-V will be available in the near future.

During the comparisons of SIF simulations with the coupled SCOPE and MODTRAN models and the DART model, the correction factor for fluorescence quantum efficiency (*fqe*) of PSII is fixed as 1 because this factor is calculated differently in these models. In the WPS model, the factor (φ_f) is determined by the incident PAR as proposed by Rosema et al. (1998). In the SCOPE model, the correction factor for *fqe* of PSII is noted as η. There are two options for the determination of η. When the energy balance module is switched on, two methods are available for the user to choose to calculate η: 1) the empirical model by van der Tol et al. (2014); 2) the model by Magnani et al. (2009). The values of η for sunlight and shaded leaves are separately calculated. When the energy balance module is switched off, η for both sunlight and shaded leaves is fixed as 1, i.e. no correction made for *fqe* of PSII. In the DART model for the correction of *fqe* for PSII, a vertical *eta* profile can be inserted either for a whole canopy, per a foliage group, or per pre-defined leaf groups (Malenovský et al., 2021). Since DART does not contain soil-vegetation-atmosphere transfer (SVAT) of energy, the *eta* parameter must be pre-computed out of DART with a SVAT model, e.g. SCOPE. If the *eta* weighting is not switched on, no correction is made, i.e. *eta* equal to 1. It can be seen that the three models adopt different methods to model or parameterize the correction factor for *fqe* of PSII. Besides, all of them have the option that no correction is made for *fqe* of PSII. To reduce the uncertainty of SIF simulations among the three models when implementing the different correction schemes for *fqe* of PSII, and focus on the evaluations of the RT for the excited fluorescence photons, we start from the baseline scenario, i.e. fixed value of 1. Otherwise, the differences of SIF simulations among the three models can arise from either the RT module or the modeling of φ_f, η, or *eta*, with the latter out of the scope of the current paper.

Among the RT models that can model the radiative coupling between the atmosphere and the land surface to simulate the SIF signal received by sensors from TOC up until TOA at a relatively high spectral resolution, e.g. $\leq$ 1 nm, the WPS model is applicable to more complex 3-D canopy structures than the SCOPE model, and is computationally less demanding than DART-FT (flux tracking module), especially with the TM module introduced in this study. For the scenario with trees represented as 3-D arrays of voxels containing turbid medium in Section 3.3 for DART, it takes 257 h 30 min/69 h 19 min for the simulation of TOA radiance spectra with SIF at nadir from 400 to 850 nm with a spectral resolution of 0.5 nm/1 nm on a Windows-based computer with a CPU (Central Processing Unit) core (Intel Skylake) @2.10 GHz, with the usage of runtime memory around 64 Gigabytes. As a comparison, it takes 12 h 12 min/3 h 49 min and 718 Megabytes (MB)/360 MB for the WPS model with the module of explicit canopy structure (noted as "ES") representation with a spectral resolution of 0.5 nm/1 nm on the same computer platform. The computer time further reduces to 39 min/21 min for the WPS model with the TM module simulated at 0.5 nm/1 nm resolution, with the memory usage of 713 MB/362 MB. However, since the scene used for the intercomparisons with the DART model is relatively small with a total of 21 $\times$ 1200 = 25,200 leaf disks, the advantage of less memory usage by the TM module cannot be testified in the above comparison. Therefore, we add one more comparison for the ROMC scene HET01_DIS_UNI with 15 $\times$ 50,000 = 750,000 leaf disks, which is the scene with largest number of facets adopted in this study.

The radiance spectra with SIF at nadir at both TOC and TOA levels with the spectral resolutions of 0.15, 0.5, and 1 nm on the same computer platform are simulated for HET01_DIS_UNI using the ES and TM modules in WPS, which shows they agree with each other closely as presented in Section 6 of the Supplementary Data. The computational costs by the two modules are provided in Table 4. It takes more than two times of computation time by ES than that by TM to simulate the TOA radiance spectrum at the same spectral resolution. The memory usage by the ES module is always higher than that by the TM module at the same resolution for the three spectral resolutions. This higher memory consumption by ES arises mainly from the storage of the facets with various attributes, e.g., positions, element's category, and optical properties. Even though the saving of memory usage is modest (~280 MB) due to the relatively small scene (750,000 disks), the advantage of less memory usage by the TM module is verified.

The much less time and memory required by WPS, especially for the TM module, make it suitable to be run on a common personal computer. It should be noted that the DART model is also improved with its computational efficiency. A new module, DART-Lux, by adopting a bidirectional MC modeling approach, can reduce computer time and memory by a hundredfold compared to DART-FT (Wang et al., 2022). Although DART-Lux already simulates most remote sensing products of DART-FT, the simulation of the SIF signal at TOA with the atmosphere interference is still under development (Wang et al., 2022).

It is also important to evaluate the performance of the WPS model under real experimental conditions, besides the model intercomparisons with the numerical RT models. We designed and performed hyperspectral measurements of a rapeseed crop by targeting the same location through UAV, with matching canopy spectral and structural data and

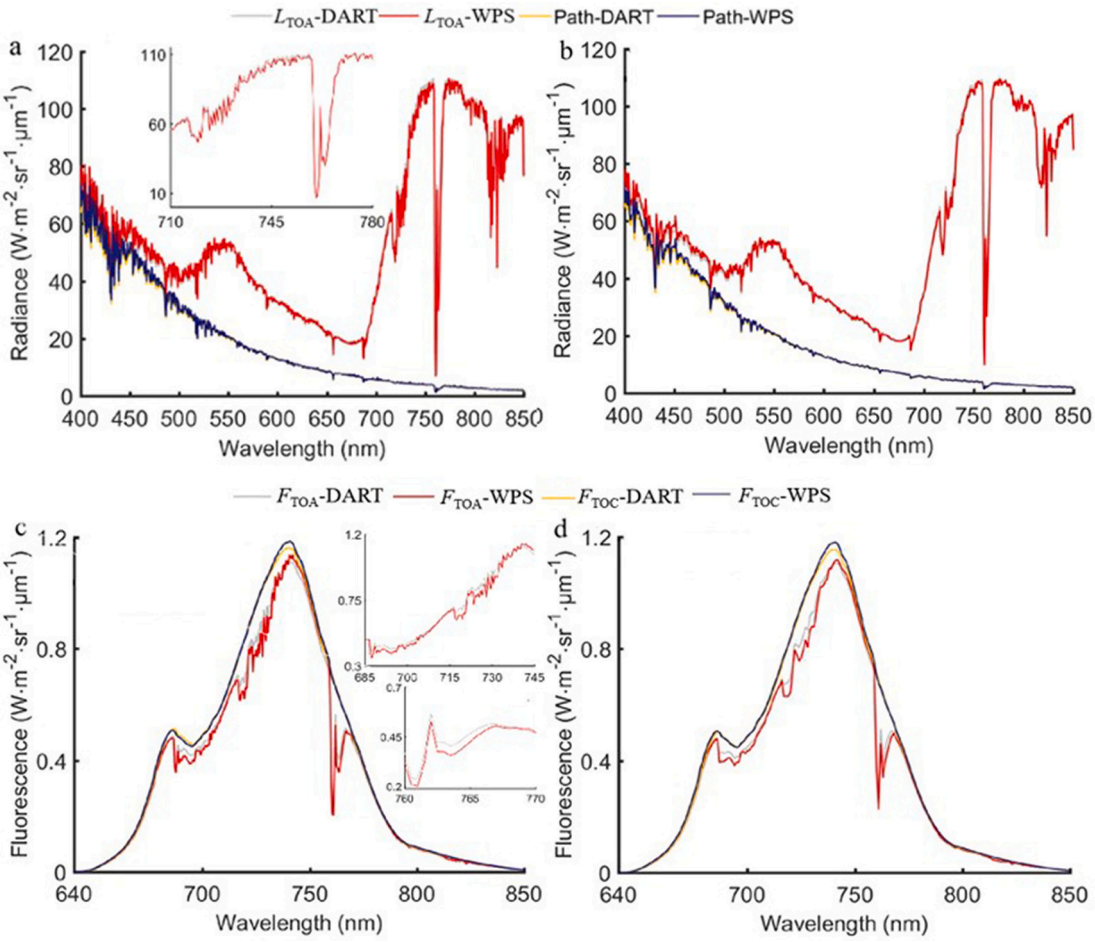

Fig. 7. Spectral distributions of TOA path radiation (Path) and total radiance (L_{TOA}), TOC SIF (F_{TOC}) and TOA total SIF (F_{TOA}) simulated by WPS and the DART model for the heterogeneous 3-D canopies at resolutions of 0.5 nm (a and c, left column) and 1 nm (b and d, right column).

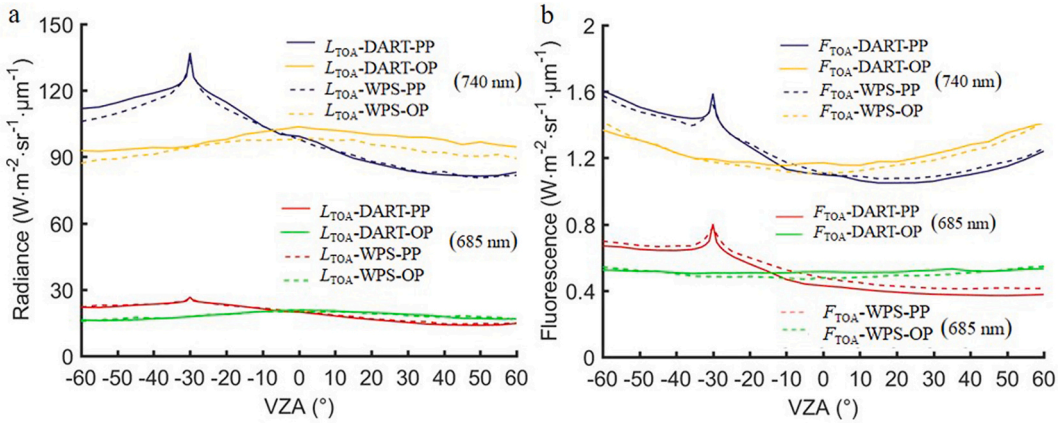

Fig. 8. Angular distributions of TOA total radiance (L_{TOA}, a) and SIF (F_{TOA}, b) at 685 nm and 740 nm along the solar principal plane (PP) and orthogonal plane (OP) simulated by WPS (dashed line) and the DART model (solid line) for the heterogeneous 3-D canopies.

atmospheric parameters required by the WPS model. We compared the simulated total radiance spectra at two AGL altitudes with the corresponding measured ones. Ideally, SIF values simulated by the model and the retrieved should also be compared. However, a reliable SIF retrieval from airborne data needs accurate knowledge of atmospheric conditions (Daumard et al., 2015), e.g., aerosol model, pressure, temperature, and water content, or requires the existence of non-fluorescent reference surfaces in close vicinity to the vegetation targets, measured at the same illumination/observation geometry (Damm et al., 2014). Unfortunately, we did not carry out either experiment in this study due to logistical and experimental limitations. Considering the limited samples of canopy type and location and the inadequate supplementary measurements, more systematic experimental data obtained by airborne or spaceborne hyperspectral sensors should be employed to fully evaluate the WPS model.

Currently the atmosphere in WPS is assumed to be 1-D, containing

Table 3
Statistical results of correlation between WPS and the DART model for the 3-D canopy scene coupled with homogeneous atmosphere.

Statistical indicators		
L_{TOA} (TOA, at nadir)	R^2	0.998 [a] 0.999 [b]
	RMSE	1.175 1.065
	AARE	1.591% 1.578%
Path radiance (at nadir)	R^2	0.999 0.999
	RMSE	0.798 0.740
	AARE	2.194% 1.988%
F_{TOA} (TOA, at nadir)	R^2	0.997 0.998
	RMSE	0.019 0.018
	AARE	3.438% 3.191%
L_{TOA} (TOA, in PP and OP)	R^2	0.984 [c] 0.973 [d]
	RMSE	0.470 3.326
	AARE	2.099% 2.644%
F_{TOA} (TOA, in PP and OP)	R^2	0.923 0.966
	RMSE	0.032 0.029
	AARE	5.918% 1.961%

[a] Values of the statistical indicators at 0.5 nm resolution;
[b] Values of the statistical indicators at 1 nm resolution;
[c] Values of the statistical indicators at 685 nm;
[d] Values of the statistical indicators at 740 nm;

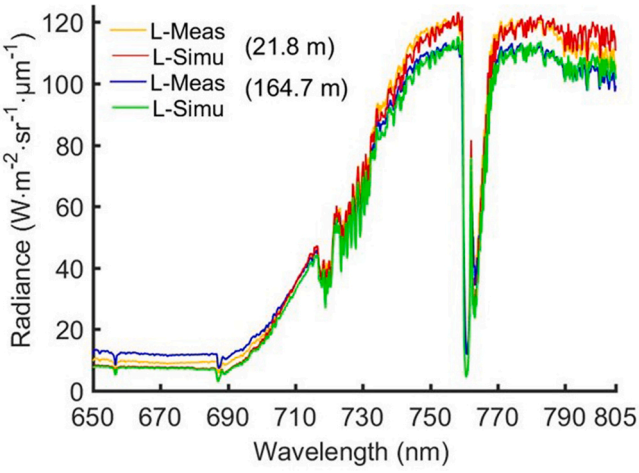

Fig. 9. Radiance spectra measured by the UAV system (L-Meas) and simulated by the WPS model (L-Simu) at two altitudes above ground level.

only gases and aerosols. Nevertheless, studies show that a sufficient amount of far-red SIF can be observed by the satellite even in the presence of optically thin or moderate amounts of broken clouds (Frankenberg et al., 2012; Köhler et al., 2015; Guanter et al., 2015). Cloudy atmosphere has typically complex 3-D structures. Therefore, the atmosphere module in WPS should be improved to describe 3-D clouds so as to study the impact of clouds on the transfer of SIF under cloudy conditions. Since the MC method has been widely applied in the RT modeling of 3-D clouds (Marchuk et al., 1980), the improvement will not be so difficult once 3-D input data (e.g. structure and optical properties) of the cloudy atmospheres are available.

Table 4
Computational costs for the simulation of TOA radiance spectra by the modules of the explicit canopy structure representation (ES) and the turbid medium representation (TM) in WPS at different spectral resolutions for the ROMC scene HET01_DIS_UNI.

Computational cost		0.15 nm	0.5 nm	1 nm
Computation time	ES	164 h 8 min	23 h 31 min	8 h 19 min
	TM	2 h 31 min	40 min	21 min
Runtime memory usage	ES	2533 MB	971 MB	629 MB
	TM	2248 MB	696 MB	341 MB

SIF emission from plants is dynamically regulated by the photochemical and non-photochemical processes responding to light intensities and other environmental conditions. At present, the regulation of SIF emission is considered with the correction of *fqe* for PSII by φ_f, which is simplified as a function of irradiance as proposed by Rosema et al. (1998). To fully consider the regulations between fluorescence emission efficiency and photosynthetic light use efficiency under various environmental conditions, a dedicated module to compute the energy balance of net radiation, sensible and latent heat flux, ground heat flux and photosynthesis inside the 3-D canopy, is needed, which will be included in our future work.

Though the evaluations of WPS by two well-established models are performed to simulate hyperspectral measurements for limited scenarios of coupled canopy and atmosphere, this endeavor represents the first attempt to inter-compare SIF simulations at both TOC and TOA levels based on different formulations and demonstrates encouraging consistencies between WPS and the other two models. A leap forward can be initiated to assess the uncertainties for existing SIF models in order to establish the consensus among the SIF modeling community. To achieve this goal, more systematic intercomparisons under well-controlled experimental conditions with well-designed protocols should be performed, as implemented in RAMI exercises for canopy reflectance models. With recent theoretical and modeling achievements, the SIF modeling community is reaching a point where the uncertainties of the RT models should be inter-compared, evaluated and further decreased. Fortunately, such an intercomparison exercise for SIF models is under consideration (Z. Malenovský, personal communication). The intercomparison results in this study can be a good start to the initiative.

6. Conclusions

In this paper, we introduced major extensions of the WPS model and systematic evaluation of the new modules. By modeling the radiative coupling between atmosphere and land surface with the same MCRT method, the non-fluorescent and SIF radiance received by sensors can be simulated from TOC to TOA levels in a coherent manner. Instead of the explicit description of architecturally realistic canopies with large numbers of facets requiring extensive computer resources, new extension to represent the 3-D canopies with geometrical primitives composed of turbid medium makes the hyperspectral simulation (especially SIF) for a sensor with medium spatial resolution at kilometer-scale feasible and practical on a common personal computer. Both methods to represent the 3-D canopy have been coupled with the atmospheric module in WPS, which can suit for different application requirements.

The performance for simulating the radiative coupling between vegetation and atmosphere in WPS is firstly evaluated by detailed comparison with the coupled SCOPE and MODTRAN models for 1-D atmosphere over two homogeneous canopies at two spectral resolutions (0.15 nm and 1 nm). Then WPS is further compared with the DART model for 1-D atmosphere above a 3-D heterogeneous canopy, also at two spectral resolutions (0.5 nm and 1 nm). These detailed comparisons among models demonstrate that they agree fairly well with each other,

with the deviations explanatory due to the different parameterizations and formulations of the models. Hyperspectral measurements through UAV at two AGL altitudes were also used to evaluate the WPS model under real experimental conditions. The simulated radiance spectra by WPS can reproduce the measured ones of a rapeseed crop and capture the trends for different AGL altitudes.

WPS can be used as a versatile tool to assess the impacts of various factors, e.g., canopy 3-D structure, leaf biochemical properties, and atmospheric conditions, on the SIF signal for wide classes of vegetation canopies. Besides, with the extension of the 3-D representation of heterogeneous plant structure and the atmospheric module over large scale scenes, hyperspectral radiance spectrum observed by spaceborne spectrometers can be simulated, together with the SIF signal both at TOC and TOA levels. With this kind of simulations, various SIF retrieval approaches can be evaluated by the known reference SIF values, which is the key problem for the assessment of current SIF product because of the unknown true values. The WPS model will be expected to contribute to these topics in future studies.

Credit author statement

Feng Zhao: Conceptualization, Data curation, Formal analysis, Methodology, Project administration, Software, Validation, Writing - original draft, Review & editing, Funding acquisition. Zhenjiang Li: Formal analysis, Methodology, Software, Validation, Writing-Review & editing. Wout Verhoef: Formal analysis, Methodology, Software, Validation, Writing-Review & editing. Chongrui Fan: Formal analysis, Methodology, Software, Validation. Hexuan Luan: Software, Validation. Tiangang Yin: Formal analysis, Validation, Writing-Review & editing. Jian Zhan: Data curation. Zhunqiao Liu: Data curation, Writing-Review & editing. Chiming Tong: Validation. Yunfei Bao: Writing-Review & editing, Funding acquisition.

Declaration of Competing Interest

The authors declare that they have no known competing financial interests or personal relationships that could have appeared to influence the work reported in this paper.

Acknowledgements

This work was supported by the Chinese Natural Science Foundation (Grant Nos. 41771382, 41401410, 41611530544). We thank our group members for their help in the field work. We thank the three reviewers for their helpful comments.

Appendix A. Supplementary data

Supplementary data to this article can be found online at https://doi.org/10.1016/j.rse.2022.113075.

References

Ångström, A., 1964. The parameters of atmospheric turbidity. Tellus 16, 64–75.
Bailey, B.N., 2019. Helios: a scalable 3D plant and environmental biophysical modeling framework. Front. Plant Sci. 10, 1185.
Berk, A., Anderson, G.P., Acharya, P.K., Chetwynd, J.H., Bernstein, L.S., Shettle, E.P., Matthew, M.W., Adler-Golden, S.M., 2000. MODTRAN4 User's Manual. Air Force Research Laboratory, Space Vehicles Directorate, Air Force Materiel Command, Hanscom AFB. MA 01731–3010, 97 pp.
Borel, C.C., Gerstl, S., Powers, B., 1991. The radiosity method in optical remote sensing of structured 3-D surfaces. Remote Sens. Environ. 36, 13–44.
Chandrasekhar, S., 1950. Radiative Transfer. Clarendon Press, Oxford.
Cogliati, S., Verhoef, W., Kraft, S., Sabater, N., Alonso, L., Vicent, J., Moreno, J., Drusch, M., Colombo, R., 2015. Retrieval of sun-induced fluorescence using advanced spectral fitting methods. Remote Sens. Environ. 169, 344–357.
Damm, A., Guanter, L., Laurent, V.C., Schaepman, M.E., Schickling, A., Rascher, U., 2014. FLD-based retrieval of sun-induced chlorophyll fluorescence from medium spectral resolution airborne spectroscopy data. Remote Sens. Environ. 147, 256–266.
Daumard, F., Champagne, S., Fournier, A., Goulas, Y., Ounis, A., Hanocq, J.F., Moya, I., 2010. A field platform for continuous measurement of canopy fluorescence. IEEE Trans. Geosci. Remote Sens. 48 (9), 3358–3368.
Daumard, F., Goulas, Y., Ounis, A., Pedrós, R., Moya, I., 2015. Measurement and correction of atmospheric effects at different altitudes for remote sensing of sun-induced fluorescence in oxygen absorption bands. IEEE Trans. Geosci. Remote Sens. 53 (9), 5180–5196.
Dubovik, O., King, M.D., 2000. A flexible inversion algorithm for retrieval of aerosol optical properties from sun and sky radiance measurements. J. Geophys. Res. 105, 20673–20696.
Frankenberg, C., Berry, J., 2018. Solar induced chlorophyll fluorescence: Origins, relation to photosynthesis and retrieval. In: Reference Module in Earth Systems and Environmental Sciences, vol. 3. Elsevier, pp. 143–162.
Frankenberg, C., O'Dell, C., Guanter, L., McDuffie, J., McDuffie, J., 2012. Remote sensing of near-infrared chlorophyll fluorescence from space in scattering atmospheres: implications for its retrieval and interferences with atmospheric CO2 retrievals. Atmos. Meas. Tech. 5 (8), 2081–2094.
Garzonio, R., Di Mauro, B., Colombo, R., Cogliati, S., 2017. Surface reflectance and sun-induced fluorescence spectroscopy measurements using a small hyperspectral UAS. Remote Sens. 9 (5), 472.
Gastellu-Etchegorry, J.P., Demarez, V., Pinel, V., Zagolski, F., 1996. Modeling radiative transfer in heterogeneous 3-D vegetation canopies. Remote Sens. Environ. 58, 131–156.
Gastellu-Etchegorry, J.P., Lauret, N., Yin, T., Landier, L., Kallel, A., Malenovský, Z., Bitar, A.A., Aval, J., Benhmida, S., Qi, J., Medjdoub, G., Guilleux, J., Chavanon, E., Cook, B., Morton, D., Chrysoulakis, N., Mitraka, Z., 2017. DART: recent advances in remote sensing data modeling with atmosphere, polarization, and chlorophyll fluorescence. IEEE J. Sel. Top. Appl. Earth Obs. Remote Sens. 10, 2640–2649.
Goel, N.S., 1988. Models of vegetation canopy reflectance and their use in estimation of biophysical parameters from reflectance data. Remote Sens. Rev. 4, 1–222.
Goel, N., Rozehnal, I., Thompson, R., 1991. A computer graphics based model for scattering from objects of arbitrary shapes in the optical region. Remote Sens. Environ. 36, 73–104.
Grau, E., Gastellu-Etchegorry, J.P., 2013. Radiative transfer modeling in the Earth–Atmosphere system with DART model. Remote Sens. Environ. 139, 149–170.
Guanter, L., Aben, I., Tol, P., Krijger, J.M., Hollstein, A., Köhler, P., Landgraf, J., 2015. Potential of the TROPOspheric monitoring instrument (TROPOMI) onboard the Sentinel-5 precursor for the monitoring of terrestrial chlorophyll fluorescence. Atmos. Meas. Tech. 8 (3), 1337–1352.
Gupana, R.S., Odermatt, D., Cesana, I., Giardino, C., Nedbal, L., Damm, A., 2021. Remote sensing of sun-induced chlorophyll-a fluorescence in inland and coastal waters: current state and future prospects. Remote Sens. Environ. 262, 112482.
Hernández-Clemente, R., North, P.R.J., Hornero, A., Zarco-Tejada, P.J., 2017. Assessing the effects of forest health on sun-induced chlorophyll fluorescence using the FluorFLIGHT 3-D radiative transfer model to account for forest structure. Remote Sens. Environ. 193, 165–179.
Hornero, A., North, P.R.J., Zarco-Tejada, P.J., Rascher, U., Martín, M.P., Migliavacca, M., Hernandez-Clemente, R., 2021. Assessing the contribution of understory sun-induced chlorophyll fluorescence through 3-D radiative transfer modelling and field data. Remote Sens. Environ. 253, 112195.
Ishimaru, A., 1978. Wave propagation and scattering in random media. In: Single Scattering and Transport Theory, vol. 1. Academic Press, New York.
Iwabuchi, H., 2006. Efficient Monte Carlo methods for radiative transfer modeling. J. Atmos. Sci. 63, 2324–2339.
Kobayashi, H., Iwabuchi, H., 2008. A coupled 1-D atmosphere and 3-D canopy radiative transfer model for canopy reflectance, light environment, and photosynthesis simulation in a heterogeneous landscape. Remote Sens. Environ. 112, 173–185.
Köhler, P., Guanter, L., Joiner, J., 2015. A linear method for the retrieval of sun-induced chlorophyll fluorescence from GOME-2 and SCIAMACHY data. Atmos. Meas. Tech. 8 (6), 2589–2608.
Kuusk, A., 1991. The hot spot effect in plant canopy reflectance. In: Myneni, R.B., Ross, J. (Eds.), Photon–Vegetation Interactions. Applications in Optical Remote Sensing and Plant Ecology. Springer-Verlag, Berlin, pp. 139–159.
Kuusk, A., 2018. Canopy radiative transfer modeling. Compr. Remote Sens. 9–22.
LI-COR Inc, 2012. LAI-2200 Plant Canopy Analyzer Instruction Manual. Lincoln, Nebraska.
Liou, K.N., 2002. An Introduction to Atmospheric Radiation. Academic Press.
Liu, X., Guanter, L., Liu, L., Damm, A., Malenovský, Z., Rascher, U., Peng, D., Du, S., Gastellu-Etchegorry, J.-P., 2018. Downscaling of solar-induced chlorophyll fluorescence from canopy level to photosystem level using a random forest model. Remote Sens. Environ. 231, 110772.
Liu, W., Atherton, J., Mõttus, M., Gastellu-Etchegorry, J.-P., Malenovský, Z., Raumonen, P., Åkerblom, M., Mäkipää, R., Porcar-Castell, A., 2019. Simulating solar-induced chlorophyll fluorescence in a boreal forest stand reconstructed from terrestrial laser scanning measurements. Remote Sens. Environ. 232, 111274.
Lu, X., Liu, Z., Zhao, F., Tang, J., 2020. Comparison of total emitted solar-induced chlorophyll fluorescence (SIF) and top-of-canopy (TOC) SIF in estimating photosynthesis. Remote Sens. Environ. 251, 112083.
Magnani, F., Olioso, A., Demarty, J., Germain, V., Verhoef, W., Moya, I., et al., 2009. Assessment of vegetation photosynthesis through observation of solar induced fluorescence from space. In: ESTEC Contract No. 20678/07/NL/HE, Final Report.
Malenovský, M., Regaieg, O., Yin, T., Lauret, N., Guilleux, J., Chavanon, E., Duran, N., Janoutová, R., Delavois, A., Meynier, J., Medjdoub, G., Yang, P., van der Tol, C., Morton, D., Douglas, B., Gastellu-Etchegorry, J., 2021. Discrete anisotropic radiative transfer modelling of solar-induced chlorophyll fluorescence: structural impacts in geometrically explicit vegetation canopies. Remote Sens. Environ. 263, 112564.

Marchuk, G.I., Mikhailov, G.A., Nazaraliev, M.A., Darbinjan, R.A., Kargin, B.A., Elepov, B.S., 1980. The Monte Carlo Methods in Atmospheric Optics, Springer Series in Optical Sciences. Springer, Berlin.

Marrs, J.K., Jones, T.S., Allen, D.W., Hutyra, L.R., 2021. Instrumentation sensitivities for tower-based solar-induced fluorescence measurements. Remote Sens. Environ. 259, 112413.

Miller, J., Berger, M., Goulas, Y., Jacquemoud, S., Louis, J., Mohammed, G., Noise, N., Moreno, J., Moya, I., Pédros, R., Verhoef, W., Zarco-Tejada, P., 2005. Development of a Vegetation Fluorescence Canopy Model, Final Report. ESA/ESTEC Contract No. 16365/02/NL/FF.

Mohammed, G.H., Colombo, R., Middleton, E.M., Rascher, U., van der Tol, C., Nedbal, L., Goulas, Y., 2019. Remote sensing of solar-induced chlorophyll fluorescence (SIF) in vegetation: 50 years of progress. Remote Sens. Environ. 231, 111177.

North, P.R.J., 1996. Three-dimensional forest light interaction model using a Monte Carlo method. IEEE Trans. Geosci. Remote Sens. 34, 946–956.

Porcar-Castell, A., Tyystjärvi, E., Atherton, J., Van der Tol, C., Flexas, J., Pfündel, E.E., Moreno, J., Frankenberg, C., Berry, J.A., 2014. Linking chlorophyll a fluorescence to photosynthesis for remote sensing applications: mechanisms and challenges. J. Exp. Bot. 65, 4065–4095.

Porcar-Castell, A., Malenovský, Z., Magney, T., et al., 2021. Chlorophyll-a fluorescence illuminates a path connecting plant molecular biology to earth-system science. Nat. Plant 7 (8), 998–1009. https://doi.org/10.1038/s41477-021-00980-4.

Rahman, H., Pinty, B., Verstraete, M.M., 1993. Coupled surface-atmosphere reflectance (CSAR) model: 2. Semiempirical surface model usable with NOAA advanced very high resolution radiometer data. J. Geophys. Res.-Atmos. 98 (D11), 20791–20801.

Rascher, U., Alonso, L., Burkart, A., Cilia, C., Cogliati, S., Colombo, R., Zemek, F., 2015. Sun-induced fluorescence–a new probe of photosynthesis: first maps from the imaging spectrometer HyPlant. Glob. Chang. Biol. 21 (12), 4673–4684.

Rosema, A., Snel, J.F.H., Zahn, H., Buurmeijer, W.F., Van Hove, L.W.A., 1998. The relation between laser-induced chlorophyll fluorescence and photosynthesis. Remote Sens. Environ. 65, 143–154.

Ross, J.K., 1981. The Radiation Regime and Architecture of Plant Stands. W. Junk Publ, The Hague.

Sabater, N., Vicent, J., Alonso, L., Verrelst, J., Middleton, E.M., Porcar-Castell, A., Moreno, J., 2018. Compensation of oxygen transmittance effects for proximal sensing retrieval of canopy–leaving sun–induced chlorophyll fluorescence. Remote Sens. 10 (10), 1551.

Sakai, Y., Kobayashi, H., Kato, T., 2020. FLiES-SIF version 1.0: three-dimensional radiative transfer model for estimating solar induced fluorescence. Geosci. Model Dev. 13, 4041–4066.

Shultis, J.K., Myneni, R.B., 1988. Radiative transfer in vegetation canopies with anisotropic scattering. J. Quant. Spectrosc. Radiat. Transf. 39, 115–129.

Tong, C., Bao, Y., Zhao, F., Fan, C., Li, Z., Huang, Q., 2021. Evaluation of the FluorWPS model and study of the parameter sensitivity for simulating solar-induced chlorophyll fluorescence. Remote Sens. 13 (6), 1091.

van der Tol, C., Verhoef, W., Timmermans, J., Verhoef, A., Su, Z., 2009. An integrated model of soil-canopy spectral radiances, photosynthesis, fluorescence, temperature and energy balance. Biogeosciences 6, 3109–3129.

van der Tol, C., Berry, J.A., Campbell, P.K.E., Rascher, U., 2014. Models of fluorescence and photosynthesis for interpreting measurements of solar-induced chlorophyll fluorescence. J. Geophys. Res. Biogeosci. 119 (12), 2312–2327.

van der Tol, C., Vilfan, N., Dauwe, D., Cendrero-Mateo, M.P., Yang, P., 2019. The scattering and re-absorption of red and near-infrared chlorophyll fluorescence in the models Fluspect and SCOPE. Remote Sens. Environ. 232, 111292.

van Wittenberghe, S., Alonso, L., Verrelst, J., Hermans, I., Delegido, J., Veroustraete, F., Samson, R., 2013. Upward and downward solar-induced chlorophyll fluorescence yield indices of four tree species as indicators of traffic pollution in Valencia. Environ. Pollut. 173, 29–37.

Verhoef, W., 1984. Light scattering by leaf layers with application to canopy reflectance modeling: the SAIL model. Remote Sens. Environ. 6, 125–184.

Verhoef, W., 1985. Earth observation modeling based on layer scattering matrices. Remote Sens. Environ. 17, 165–178.

Verhoef, W., 1998. Theory of Radiative Transfer Models Applied in Optical Remote Sensing of Vegetation Canopies. Ph.D. thesis. Wageningen Agricultural University, The Netherlands.

Verhoef, W., Bach, H., 2007. Coupled soil–leaf-canopy and atmosphere radiative transfer modeling to simulate hyperspectral multi-angular surface reflectance and TOA radiance data. Remote Sens. Environ. 109 (2), 166–182.

Verhoef, W., Bach, H., 2012. Simulation of Sentinel-3 images by four-stream surface–atmosphere radiative transfer modeling in the optical and thermal domains. Remote Sens. Environ. 120, 197–207.

Verhoef, W., van der Tol, C., Middleton, E.M., 2018. Hyperspectral radiative transfer modeling to explore the combined retrieval of biophysical parameters and canopy fluorescence from FLEX – Sentinel-3 tandem mission multi-sensor data. Remote Sens. Environ. 204, 942–963.

Vilfan, N., van der Tol, C., Muller, O., Rascher, U., Verhoef, W., 2016. Fluspect-B: a model for leaf fluorescence, reflectance and transmittance spectra. Remote Sens. Environ. 186, 596–615.

Wang, Y., Kallel, A., Yang, X., Regaieg, O., Lauret, N., Guilleux, J., Gastellu-Etchegorry, J.P., 2022. DART-Lux: an unbiased and rapid Monte Carlo radiative transfer method for simulating remote sensing images. Remote Sens. Environ. 274, 112973. https://doi.org/10.1016/j.rse.2022.112973.

Widlowski, J.-L., Robustelli, M., Disney, M., Gastellu-Etchegorry, J.-P., Lavergne, T., Lewis, P., North, P.J.R., Pinty, B., Thompson, R., Verstraete, M.M., 2008. The RAMI On-line Model Checker (ROMC): a web-based benchmarking facility for canopy reflectance models. Remote Sens. Environ. 112 (3), 1144–1150.

Yang, P., van der Tol, C., 2018. Linking canopy scattering of far-red sun-induced chlorophyll fluorescence with reflectance. Remote Sens. Environ. 209, 456–467.

Yang, P., Verhoef, W., van der Tol, C., 2017. The mSCOPE model: a simple adaptation to the SCOPE model to describe reflectance, fluorescence and photosynthesis of vertically heterogeneous canopies. Remote Sens. Environ. 201, 1–11.

Yin, T., Gastellu-Etchegorry, J.-P., Lauret, N., Grau, E., Rubio, J., 2013. A new approach of direction discretization and oversampling for 3D anisotropic radiative transfer modeling. Remote Sens. Environ. 135, 213–223.

Zeng, Y., Badgley, G., Chen, M., Li, J., Berry, J., 2020. A radiative transfer model for solar induced fluorescence using spectral invariants theory. Remote Sens. Environ. 240, 111678.

Zhao, F., Gu, X., Verhoef, W., Wang, Q., Yu, T., Liu, Q., Huang, H., Qin, W., Chen, L., Zhao, H., 2010. A spectral directional reflectance model of row crops. Remote Sens. Environ. 114 (2), 265–285.

Zhao, F., Li, Y., Dai, X., Verhoef, W., Guo, Y., Shang, H., Gu, X., Huang, Y., Yu, T., Huang, J., 2015. Simulated impact of sensor field of view and distance on field measurements of bidirectional reflectance factors for row crops. Remote Sens. Environ. 156, 129–142.

Zhao, F., Dai, X., Verhoef, W., Guo, Y., van der Tol, C., Li, Y., Huang, Y., 2016. FluorWPS: a Monte Carlo ray-tracing model to compute sun-induced chlorophyll fluorescence of three-dimensional canopy. Remote Sens. Environ. 187, 385–399.

Zhao, F., Li, R., Qin, W., Ding, W., 2018a. A model to simulate the radiative transfer of solar-induced fluorescence for three-dimensional canopies. In: 2018 IEEE International Geoscience and Remote Sensing Symposium, pp. 6003–6006.

Zhao, F., Li, R., Verhoef, W., Cogliati, S., Liu, X., Huang, Y., Guo, Y., Huang, J., 2018b. Reconstruction of the full spectrum of solar-induced chlorophyll fluorescence: intercomparison study for a novel method. Remote Sens. Environ. 219, 233–246.

Zhao, F., Ma, W., Köhler, P., Ma, X., Sun, H., Verhoef, W., Zhao, J., et al., 2022. Retrieval of red solar-induced chlorophyll fluorescence with TROPOMI on the Sentinel-5 precursor mission. IEEE Trans. Geosci. Remote Sens. 60, 1–14. https://doi.org/10.1109/TGRS.2022.3162726.